International Journal of Plasticity 66 (2015) 46–70

Contents lists available at ScienceDirect

International Journal of Plasticity

journal homepage: www.elsevier.com/locate/ijplas

A generic anisotropic continuum damage model integration scheme adaptable to both ductile damage and biological damage-like situations

M. Mengoni *, J.P. Ponthot

University of Liege (ULg), Department of Aerospace and Mechanical Engineering, Non-linear Computational Mechanics (MN²L), Liège, Belgium

ARTICLE INFO

Article history:
Received 30 September 2013
Received in final revised form 18 February 2014
Available online 9 May 2014

Keywords:
Continuum damage mechanics
B. Anisotropic material
B. Elastic–plastic material
B. Constitutive behaviour
C. Numerical algorithms

ABSTRACT

This paper aims at presenting a general versatile time integration scheme applicable to anisotropic damage coupled to elastoplasticity, considering any damage rate and isotropic hardening formulations. For this purpose a staggered time integration scheme in a finite strain framework is presented, together with an analytical consistent tangent operator. The only restrictive hypothesis is to work with an undamaged isotropic material, assumed here to follow a J_2 plasticity model. The only anisotropy considered is thus a damage-induced anisotropy. The possibility to couple any damage rate law with the present algorithm is illustrated with a classical ductile damage model for aluminium, and a biological damage-like application. The later proposes an original bone remodelling law coupled to trabecular bone plasticity for the simulation of orthodontic tooth movements. All the developments have been considered in the framework of the implicit non-linear finite element code Metafor (developed at the LTAS/MN²L, University of Liège, Belgium – www.metafor.ltas.ulg.ac.be).

1. Introduction

Damage mechanics deals with modelling the loss of stiffness and progressive microscopic failure mechanisms induced by external loading in a material. Coupled damage models are models in which damage is incorporated into constitutive equations. Their use can lead to the development of complex constitutive equations whose numerical integration has to be considered adequately.

Two main coupled approaches to damage mechanics can be found in the literature.

The first one is a micromechanical approach to damage based on the work of Gurson (1977) who considered the growth of spherical voids in a plastic material. The extensions to the Gurson–Tvergaard–Needlemann (GTN) model accounted for plastic hardening and physically described the ductility of materials (Tvergaard and Needleman, 1984; Rousselier, 1987). GTN models define the damage variable as the void fraction, and its evolution is due to the nucleation, growth and coalescence of voids. While initially an isotropic approach to damage, it has been extended to anisotropic damage (Hammi and Horstemeyer, 2007; Zapara et al., 2012; Horstemeyer and Bammann, 2010).

The second one is a phenomenological approach to damage often referred to as the Continuum Damage Mechanics (CDM). It should be noted however that the GTN approach is also a continuum approach to damage and thus that the

* Corresponding author. Tel.: +44 1133435011.
E-mail address: mmengoni@ulg.ac.be (M. Mengoni).

http://dx.doi.org/10.1016/j.ijplas.2014.04.005
0749-6419/

terminology CDM may be considered as improper. Phenomenological damage models based on the concept of effective stress space were introduced by Kachanov (1958) and later by Rabotnov (1968) [as cited in Voyiadjis and Kattan (2006) and Lemaitre and Desmorat (2005)] who were the first to introduce a scalar damage variable which may be interpreted as the effective surface density of micro-cracks per unit volume. The CDM is derived from a thermodynamic framework, ensuring the positivity of the dissipation. The damage variable is an internal variable related to the effective density of cracks or cavities at each point (for the isotropic case) or at each point and in each direction (anisotropic case), that is, to the microstructure. As for the GTN approach, while the CDM was initially developed considering a scalar damage variable, it has been extended to a tensor representation describing a damage-induced anisotropy (Voyiadjis et al., 2008; Desmorat and Otin, 2008; Brünig et al., 2008; Abu Al-Rub and Voyiadjis, 2003; Badreddine et al., 2010; Brodland et al., 2006; Dunand et al., 2012).

For both approaches, a description of the coupling between damage and elasto-plasticity has to be completed with a damage evolution law. While damage evolution laws were proposed in the original works deriving the GTN or CDM approaches, several other damage rate expressions can be found in the literature describing different damage mechanisms (Duddu and Waisman, 2013; Souza and Allen, 2012; Tekoglu and Pardoen, 2010; Hammi and Horstemeyer, 2007; Qi and Bertram, 1999; Kitzig and Häußler-Combe, 2011; Lecarme et al., 2011; Khan and Liu, 2012; Lai et al., 2009; Zairi et al., 2011) and coupling with time-, rate-, and temperature-dependent materials (Abu Al Rub and Darabi, 2012; Besson, 2009; Stewart et al., 2011; Horstemeyer et al., 2000; Guo et al., 2013), to cite only a few.

In the present work, we will use the phenomenological approach of anisotropic damage, i.e. anisotropic Continuum Damage Mechanics. This choice is driven by the wide range of applications of CDM. In particular, and as will be treated further in this work, it can be extended to represent a stiffness softening not linked to the growth of micro-cracks but to other phenomena, such as a bio-chemical coupling. Considering biological effects coupled to mechanical loading, we will be interested in describing the effect of biological actions on the material behaviour rather than describing in details the biological phenomena. The use of a CDM approach in this context rather than a GTN approach of damage is thus straightforward to describe the evolution of the stiffness tensor due to external loading. Besides, the coupling between elasticity and damage in those cases plays a strong role which is naturally included into the CDM approach. In the case of GTN models, the elastic properties can also be functions of damage but this dependence is often neglected.

In this work an additive decomposition of the strain rate is assumed to model the elastoplasticity in finite strains. It should however be noted that several studies also developed mathematical frameworks to couple anisotropic damage and multiplicative elastoplasticity (Menzel et al., 2005; Brünig, 2002, 2003a; Ekh et al., 2004). This approach to elastoplasticity in large strains leads to a completely different formulation of damage (Brünig, 2003b). The computational tools developed to integrate anisotropic damage in that case are thus not applicable in the present work.

The numerical integration algorithms of constitutive models incorporating anisotropic damage effects presented in the literature (Lemaitre and Desmorat, 2005; Borgqvist and Wallin, 2013; El khaoulani and Bouchard, 2013; Brünig et al., 2008; de Souza Neto et al., 2011) are usually limited to one given damage model and are not easily extended to other formulations or damage criteria. The numerical scheme in Simo and Ju (1987a,b) or in Jeunechamps and Ponthot (2013) is similar to the proposed approach in such a way that the integration can be considered as a triple operator split: elastic predictor, plastic corrector, damage corrector. However this numerical scheme was developed for isotropic damage, i.e. with a scalar equation to solve for the damage correction and direct decoupling of damage and plasticity for the plastic correction. For those two reasons, several other generic integration schemes have been proposed in the case of isotropic damage (de Souza Neto et al., 1994; de Souza Neto and Perić, 1996; Doghri, 1995; Vaz and Owen, 2001; Mashayekhi et al., 2005; Boers et al., 2005). Simo and Ju (1987a,b) also propose a numerical scheme for the integration of anisotropic damage. However, in that case, a strain-based anisotropic damage is assumed, thus leading to a different numerical approach.

The present work is aimed at developing a generic phenomenological anisotropic damage integration scheme that can be coupled with any isotropic hardening law and damage rate. The only restrictive hypothesis was to work with a material whose undamaged behaviour can be modelled with a von-Mises elasto-plastic model. The anisotropy of the material is thus only a damage-induced anisotropy. Otherwise, any thermodynamically consistent damage criterion can be used in conjunction with the proposed original staggered integration scheme. Furthermore a finite strains assumption is considered for the anisotropic continuum damage formulation thus allowing the use of the model in large strains and large rotations applications. The developed algorithm can be also coupled to damage criteria as different as criteria describing ductile damage or biological damage-like phenomena. Considering the later case, an original, enhanced extension of a small-strain elastic-damage model is developed in this work and applied to simulate a tooth displacement in an orthodontic treatment. This work thus presents an original fully coupled non-linear model of bone remodelling occurring during orthodontic tooth movement.

Beyond this introduction, this paper is divided into three main sections. The first section presents the extension of CDM to a finite strain formulation considering an anisotropic symmetric second order damage tensor. Using a second order tensor restricts the anisotropy to orthotropy. This extension makes no assumption on the damage rate except that it remains a symmetric tensor. A new implicit time integration algorithm in a finite element context is then proposed. The following two sections demonstrate the versatility of the approach. First a ductile damage model was used to verify the proposed approach by comparison to another integration scheme from the literature (de Souza Neto et al., 2011). For this, a simple uniaxial test was reproduced to compare the present results with those of Aboudi (2011). Second, a biologically driven damage model was developed. Its aim was to propose a model of orthodontic tooth movement considering biological softening and hardening of bone tissue.

1.1. Notations

Einstein summation convention is used except when indicated.

As a general rule, scalar a, σ is denoted by a light-face italic letter; second-order tensor $\boldsymbol{a}, \boldsymbol{\sigma}, \boldsymbol{D}$ is signified by boldface italic letter; fourth-order tensor $\mathbb{A}$ is identified by blackboard character. Compact tensor notation is used as much as possible. The double dot product, or double contraction, is signified with $\boldsymbol{a} : \boldsymbol{b} = a_{ij}b_{ij}$ and $[\mathbb{A} : \boldsymbol{b}]_{ij} = \mathbb{A}_{ijkl}\boldsymbol{b}_{kl}$. The dyadic product $\mathbb{A} = \boldsymbol{a} \otimes \boldsymbol{b}$ and the symmetrised outer product $\mathbb{B} = \boldsymbol{a} \underline{\otimes} \boldsymbol{b}$ are defined as $\mathbb{A}_{ijkl} = \boldsymbol{a}_{ij}\boldsymbol{b}_{kl}$ and $\mathbb{B}_{ijkl} = 1/2(\boldsymbol{a}_{ik}\boldsymbol{b}_{jl} + \boldsymbol{a}_{jl}\boldsymbol{b}_{ik})$, respectively. Letter $\boldsymbol{I}$ signifies the second-order identity tensor with the components being Kronecker-delta δ_{ij}, and $\mathbb{1}$ is the symmetric fourth-order unit deviatoric tensor: $\mathbb{1} = \boldsymbol{I} \underline{\otimes} \boldsymbol{I} - 1/3\boldsymbol{I} \otimes \boldsymbol{I}$. $|\boldsymbol{D}|$ is a tensor whose principal components are the absolute value of the principal components of $\boldsymbol{D}$: $|\boldsymbol{D}| = \sum_{i=1}^{3} |d_i| \vec{n}_i \otimes \vec{n}_i$ (no Einstein summation) with d_i and $\vec{n}_i$ the eigenvalues and eigenvectors of $\boldsymbol{D}$.

2. A staggered integration procedure for anisotropic continuum damage theory

The principles of Continuum Damage Mechanics (CDM) introduce a fictitious undamaged configuration (called the effective configuration). In this configuration the (scalar) damage is virtually removed in such a way that applying the actual loads leads to an effective stress, $\tilde{\boldsymbol{\sigma}}$, defined as (Lemaitre and Desmorat, 2005):

$$\tilde{\boldsymbol{\sigma}} = \frac{\boldsymbol{\sigma}}{1 - d} \tag{1}$$

where d is a direction independent damage variable, and $\boldsymbol{\sigma}$ is the Cauchy stress tensor.

2.1. Anisotropic continuum damage mechanics

To ensure a more general formulation of the principles of damage mechanics, the case of anisotropic damage is assumed. In this case different levels of damage are related to the principal directions of the physical space, and thus a simple scalar damage parameter is no longer sufficient to quantify damage in all directions. Instead, the anisotropy of the damage distribution in the material is here interpreted using a symmetric second-order damage tensor, $\boldsymbol{d}$.

2.1.1. Effective stress

The effective stress tensor in the case of anisotropic damage is defined in such a way that it is a function of the second order damage variable and of the stress tensor. To keep a linear relationship between the effective and actual configurations, one often writes the effective stress so that

$$\tilde{\boldsymbol{\sigma}} = \mathbb{M}(\boldsymbol{d}) : \boldsymbol{\sigma} \tag{2}$$

The fourth order tensor $\mathbb{M}$ is not a damage tensor, it simply is function of a second order damage tensor $\boldsymbol{d}$, the internal variable which is normalised and related to the current state of the microstructure. Several definitions of $\mathbb{M}$ can be found in the literature (Abu Al Rub and Voyiadjis, 2006; Lemaitre et al., 2000; Lemaitre and Desmorat, 2005; Lennon and Prendergast, 2004; Menzel et al., 2002; Voyiadjis and Kattan, 2006), we will here adopt the one proposed by Lemaitre et al. (2000):

$$\mathbb{M} = \boldsymbol{H} \underline{\otimes} \boldsymbol{H} - \frac{1}{3}\left(\boldsymbol{H}^2 \otimes \boldsymbol{I} + \boldsymbol{I} \otimes \boldsymbol{H}^2\right) + \frac{1}{9}\mathrm{tr}\left(\boldsymbol{H}^2\right)\, \boldsymbol{I} \otimes \boldsymbol{I} + \frac{1}{3}\frac{\boldsymbol{I} \otimes \boldsymbol{I}}{1 - \eta d^H} \tag{3}$$

where $d^H = \mathrm{tr}(\boldsymbol{d})/3$ is the hydrostatic damage, η is an hydrostatic sensitivity parameter, and $\boldsymbol{H}$ is the effective damage tensor defined as:

$$\boldsymbol{d} = \boldsymbol{I} - \boldsymbol{H}^{-2} \tag{4}$$

This fourth order tensor, $\mathbb{M}$, has the properties of being

- symmetric, therefore resulting in a symmetric effective stress (using a simple extension of the isotropic definition: $M_{ijkl} = \delta_{ik}[\boldsymbol{I} - \boldsymbol{d}]^{-1}_{jl}$ does not lead to a symmetric result);
- independent of the Poisson's ratio value;
- compatible with the thermodynamics in a small strain approach: existence of a state potential from which the constitutive law can be derived and of a principle of strain equivalence (the symmetrization $\mathbb{M} = \boldsymbol{I} \underline{\otimes} (\boldsymbol{I} - \boldsymbol{d})^{-1}$ is not derived from a potential);
- able to represent different effects of damage on the hydrostatic and deviatoric stresses by means of an hydrostatic sensitivity parameter, η.

Combining (2) and Eq. (3) gives an equivalent stress expressed as a function of the deviatoric part of the Cauchy stress $\boldsymbol{s}$ and pressure p by:

$$\begin{cases} \tilde{p}\boldsymbol{I} = \frac{p}{1-\eta d^H}\boldsymbol{I} = p\ \mathbb{M} : \boldsymbol{I} \\ \tilde{\boldsymbol{s}} = \mathtt{dev}(\boldsymbol{H}\boldsymbol{s}\boldsymbol{H}) = \mathbb{M} : \boldsymbol{s} \end{cases} \tag{5}$$

The definition of the effective stress Eq. (2) can be analytically inverted as:

$$\boldsymbol{\sigma} = \mathbb{M}^{-1} : \tilde{\boldsymbol{\sigma}}$$

$$\text{with } \mathbb{M}^{-1} = \boldsymbol{H}^{-1} \underline{\otimes} \boldsymbol{H}^{-1} - \frac{\boldsymbol{H}^{-2} \otimes \boldsymbol{H}^{-2}}{\mathtt{tr}\left(\boldsymbol{H}^{-2}\right)} + \frac{1}{3}\left(1 - \eta d^H\right)\boldsymbol{I} \otimes \boldsymbol{I}$$

leading to

$$\begin{cases} p\boldsymbol{I} = \left(1 - \eta d^H\right)\tilde{p}\boldsymbol{I} = \tilde{p}\ \mathbb{M}^{-1} : \boldsymbol{I} \\ \boldsymbol{s} = \boldsymbol{H}^{-1}\tilde{\boldsymbol{s}}\boldsymbol{H}^{-1} - \frac{\tilde{\boldsymbol{s}} : \boldsymbol{H}^{-2}}{\mathtt{tr}\left(\boldsymbol{H}^{-2}\right)}\boldsymbol{H}^{-2} = \mathbb{M}^{-1} : \tilde{\boldsymbol{s}} \end{cases} \tag{6}$$

2.1.2. Strain equivalence formulation of damage

The strain equivalence approach of damage relates the stress level in the damaged material with the stress in the undamaged material that leads to the same strain. This assumes the deformation behaviour is affected by damage only through the effective stress. In small strain elasticity, Hooke's law is then written:

$$\tilde{\boldsymbol{\sigma}} = \mathbb{H}^o : \boldsymbol{\varepsilon}$$

where $\mathbb{H}^o$ is Hooke's fourth order tensor of elasticity, with parameters evaluated for the undamaged material:

$$\mathbb{H}^o = K\boldsymbol{I} \otimes \boldsymbol{I} + 2G\mathbb{I}$$

with K and G respectively the bulk and shear moduli of the undamaged material.

2.2. Elasto-plasticity in finite strains

Assuming a constitutive law for the undamaged material which is not restricted to basic small strain linear elasticity, we work under a finite strain framework with an additive decomposition of the strain rate:

$$\boldsymbol{D} = \boldsymbol{D}^e + \boldsymbol{D}^p \tag{7}$$

The next assumption is to work in a corotational frame. From this point forward, all quantities are expressed in a corotational frame. In this paper, we use no distinct notation for corotational quantities. All the time derivatives noted $\dot{\cdot}$ are thus to be understood as derivatives in the corotational frame. These derivatives can be associated to objective derivatives in a fixed frame of reference. In the present case, it is equivalent to a Jaumann rate (Ponthot, 2002). Thus, in the corotational frame, we assume that the corotational effective stress rate is linked to the elastic part of the corotational strain rate by the generalised Hooke's law in an hypoelastic formulation, in such a way that:

$$\dot{\tilde{\boldsymbol{\sigma}}} = \mathbb{H}^o : \boldsymbol{D}^e \tag{8}$$

When coupling damage and plasticity, one needs to express the yield criterion as well as the hardening laws in terms of damaged variables (details can be found in Lemaitre and Desmorat (2005) and Desmorat and Otin (2008) for the small strains version or in Jeunechamps and Ponthot (2013) for an extension to finite strains of isotropic damage in a hypoelastic framework). Using a von-Mises criterion for the undamaged material leads to an equivalent stress defined in the effective stress configuration as:

$$\tilde{\sigma}_{eq}^{vM} = \sqrt{\frac{3}{2}\tilde{\boldsymbol{s}} : \tilde{\boldsymbol{s}}} \tag{9}$$

The yield function then becomes:

$$f = \tilde{\sigma}_{eq}^{vM} - \sigma_y \leq 0 \tag{10}$$

where σ_y is the (current) yield stress.

Assuming a constant damage tensor (this assumption is consistent with the staggered scheme of integration that will be described later, see Section 2.3) and a normality rule in the Cauchy stress space (it is the space where the conservation equations are fulfilled and the Clausius–Duhem inequality is respected) gives the following flow rule (details are given in Appendix A):

$$\boldsymbol{D}^p = \Lambda \boldsymbol{N} \tag{11}$$

where Λ is the consistency or flow parameter and with the deviatoric unit normal, $\boldsymbol{N}$, defined by:

$$\boldsymbol{N} = \frac{\frac{\partial f}{\partial \boldsymbol{\sigma}}}{\|\partial f/\partial \boldsymbol{\sigma}\|} = \frac{\boldsymbol{n}}{\|\boldsymbol{n}\|} \tag{12}$$

with the notation

$$\boldsymbol{n} = \mathbb{M} : \tilde{\boldsymbol{s}} = \mathtt{dev}\ (\boldsymbol{H}\check{\boldsymbol{s}}\boldsymbol{H}) \tag{13}$$

The equivalent plastic strain rate is then given by:

$$\dot{\bar{\varepsilon}}^p = \sqrt{\frac{2}{3}\boldsymbol{D}^p : \boldsymbol{D}^p} = \sqrt{\frac{2}{3}}\Lambda \tag{14}$$

The damaged equivalent plastic strain, $\bar{\varepsilon}^{p,d}$, is the internal parameter driving the plastic problem. This new parameter is conjugated to the yield limit of the material, σ_y, and defined through its rate, $\dot{\bar{\varepsilon}}^{p,d}$, as:

$$\boldsymbol{D}^p = \dot{\bar{\varepsilon}}^{p,d}\frac{\partial f}{\partial \boldsymbol{\sigma}} \Rightarrow \dot{\bar{\varepsilon}}^{p,d} = \frac{\Lambda}{\|\partial f/\partial \boldsymbol{\sigma}\|} = \sqrt{\frac{2}{3}}\Lambda\frac{\|\tilde{\boldsymbol{s}}\|}{\|\boldsymbol{n}\|}$$

Finally, the last assumption for the plastic problem is to restrict the hardening law to be isotropic:

$$\sigma_y(\bar{\varepsilon}^{p,d}) = \sigma_y^0 + h\bar{\varepsilon}^{p,d}$$

with $h = \frac{d\sigma_y}{d\bar{\varepsilon}^{p,d}}$ the hardening parameter and where σ_y^0 is the yield limit of the virgin material.

This plastic problem is coupled to the damage problem, defined through the damage evolution law. In this general theoretical background, we assume that the damage rate can be described with any general damage model and we simply write: $\dot{\boldsymbol{H}} = \dot{\boldsymbol{H}}(\boldsymbol{\sigma}, \boldsymbol{D}, \bar{\varepsilon}^{p,d}, \dot{\bar{\varepsilon}}^{p,d})$. It will be particularised to two specific rates further.

2.3. Time integration algorithm

The equations that are driving the coupled damage elasto-plastic problem are the definition of the yield criterion, i.e. one scalar equation, and the decomposition of the strain rate and the damage rate, i.e. two tensorial equations:

$$\begin{cases} \text{Strain rate decomposition} & \boldsymbol{D} = \boldsymbol{D}^e + \boldsymbol{D}^p \\ \text{Yield function} & f = \tilde{\sigma}_{eq}^{vM} - \sigma_y(\dot{\bar{\varepsilon}}^{p,d}, \bar{\varepsilon}^{p,d}) \leq 0 \\ \text{Effective damage tensor evolution} & \dot{\boldsymbol{H}} = \dot{\boldsymbol{H}}(\boldsymbol{\sigma}, \boldsymbol{D}, \bar{\varepsilon}^{p,d}, \dot{\bar{\varepsilon}}^{p,d}) \end{cases} \tag{15}$$

This system introduces one scalar and two tensorial unknowns, i.e. the damaged equivalent plastic strain rate $\dot{\bar{\varepsilon}}^{p,d}$, the elastic strain rate $\boldsymbol{D}^e$, and the damage evolution $\dot{\boldsymbol{H}}$. Accounting for the symmetry of $\boldsymbol{D}^e$ and $\boldsymbol{H}$, this is therefore a non-linear system of 13 scalar unknowns.

This principal system is completed with the definition of the effective stress, the constitutive model, and the plastic flow rule, i.e. 3 tensorial equations, and the definition of the damaged equivalent plastic strain rate, i.e. a scalar equation:

$$\begin{cases} \text{Definition of the effective stress} & \tilde{\boldsymbol{\sigma}} = \mathbb{M} : \boldsymbol{\sigma} \\ \text{Constitutive law} & \dot{\tilde{\boldsymbol{\sigma}}} = \mathbb{H}^o : \boldsymbol{D}^e \\ \text{Plastic flow rule} & \boldsymbol{D}^p = \Lambda\frac{\mathtt{dev}(\boldsymbol{H}\ \tilde{\boldsymbol{s}}\ \boldsymbol{H})}{\|\mathtt{dev}(\boldsymbol{H}\ \tilde{\boldsymbol{s}}\ \boldsymbol{H})\|} \\ \text{Damaged equivalent plastic strain rate} & \dot{\bar{\varepsilon}}^{p,d} = \sqrt{\frac{3}{2}}\Lambda\frac{\|\tilde{\boldsymbol{s}}\|}{\|\boldsymbol{n}\|} \end{cases} \tag{16}$$

This introduces 19 new secondary unknowns: the Cauchy stress tensor $\boldsymbol{\sigma}$ (6 unknowns), the effective stress tensor $\tilde{\boldsymbol{\sigma}}$ (6 unknowns), the plastic strain rate $\boldsymbol{D}^p$ (6 unknowns), and the flow parameter Λ (1 unknown).

Solving the system given by Eq. (15) with a fully coupled Newton–Raphson method would require to evaluate the derivatives for each of the 13 variables with respect to each other variables, i.e. 169 derivatives. The computational cost of such a method is therefore high and considered as an issue to solve such a problem. Thus, the principle of the integration scheme proposed for the present coupled problem (plasticity and anisotropic damage) is a staggered scheme. As mentioned earlier, using such a scheme allows us to derive the driving equations of the plastic problem independently from the damage evolution law. It also allows us to derive a generic resolution scheme that can be coupled to any damage rate. The complete scheme of integration, inspired from Jeunechamps and Ponthot (2013) who proposed an integration scheme for isotropic continuum damage coupled to von-Mises plasticity, can be described as follows (see Fig. 1):

- Starting from known values at time n in the corotational frame $(\boldsymbol{\sigma}_n, \boldsymbol{H}_n, \bar{\varepsilon}_n^{p,d})$ the plastic problem is solved at constant damage in the effective stress space (the procedure to solve the plastic problem is detailed hereafter). So we first determine the effective stress, $\tilde{\boldsymbol{\sigma}}_{n+1}$, and the damaged equivalent plastic strain, $\bar{\varepsilon}_{n+1}^{p,d}$.

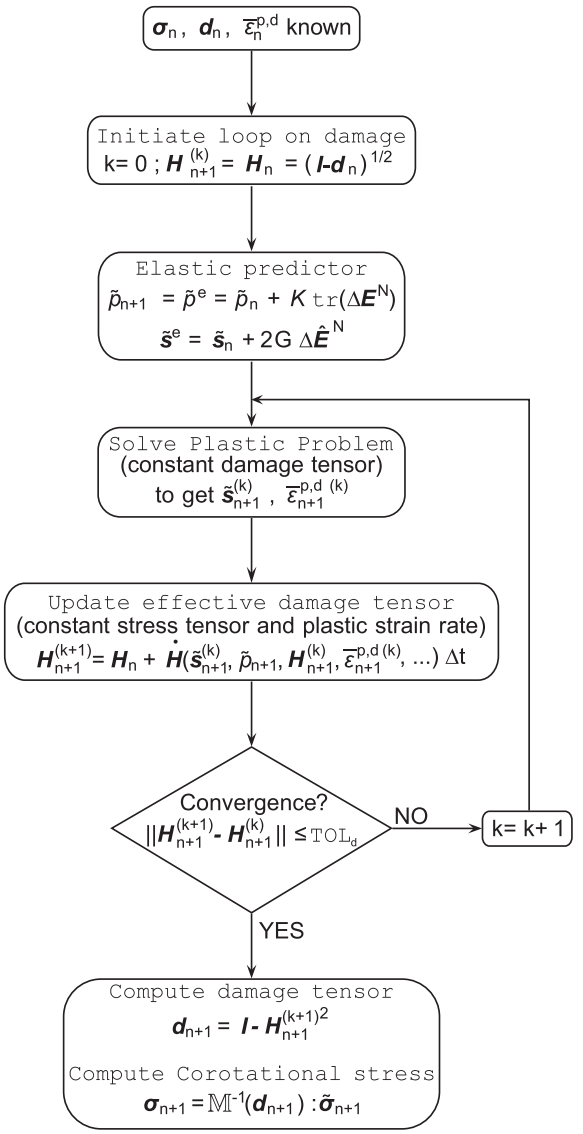

Fig. 1. Outline of the integration scheme for the coupled problem (elasto-plasticity and anisotropic damage) in the corotational frame, $\boldsymbol{\sigma}$, $\boldsymbol{d}$, $\bar{\varepsilon}^{p,d}$ are known at time step n and need to be computed for time step $n+1$. $\Delta \boldsymbol{E}^N = \mathrm{tr}\left(\Delta \boldsymbol{E}^N\right)\boldsymbol{I} + \Delta \hat{\boldsymbol{E}}^N$ is the natural strain increment over the time step, see Ponthot (2002).

- From this result, the damage evolution (through the effective damage tensor variation) is computed at constant stress and plastic strain to obtain the final value of the effective damage tensor $\boldsymbol{H}_{n+1}$. The new value of the effective damage tensor is computed using an explicit scheme on the time derivative over the time-step: $\boldsymbol{H}_{n+1} = \boldsymbol{H}_n + \dot{\boldsymbol{H}}\Delta t$ with $\dot{\boldsymbol{H}} = \dot{\boldsymbol{H}}(\tilde{\boldsymbol{\sigma}}_{n+1}, \boldsymbol{H}_n, \bar{\varepsilon}^{p,d}_{n+1}, \ldots)$ evaluated with the new effective stress and damaged equivalent plastic strain rate but with the effective damage tensor evaluated at the end of the previous time step: $\boldsymbol{H}_n$.
- This solving procedure is done iteratively, with iterations on the effective damage tensor ending when the norm of the difference between two consecutive tensors is below a user-chosen tolerance (TOL_d, chosen by default as 10^{-7}).

This stress integration problem is solved in the corotational effective stress space. The corotational Cauchy stress is then obtained simply by applying the inverse of the anisotropic damage operator on the effective stress (Eq. (6)).

The detailed algorithm used to solve the plastic problem (box "`Solve Plastic Problem`" in Fig. 1) is detailed hereafter. Using the additive decomposition of the strain rate, the constitutive law (Eq. (8)) becomes:

$$\dot{\tilde{\boldsymbol{\sigma}}} = \mathbb{H}^o : \boldsymbol{D} - \mathbb{H}^o : \boldsymbol{D}^p \tag{17}$$

As seen in Eqs. (11)–(13), the plastic strain rate is purely deviatoric and the trace of the elastic strain rate tensor is equal to the one of the total strain rate tensor.

Considering an isotropic behaviour for the undamaged material, the hydrostatic and deviatoric parts of the effective stress rate therefore become:

$$\begin{cases} \dot{\tilde{p}} = K\,\mathrm{tr}(\boldsymbol{D}) \\ \dot{\tilde{\boldsymbol{s}}} = 2G\,\mathrm{dev}(\boldsymbol{D}) - 2G\Lambda\boldsymbol{N} \end{cases} \tag{18}$$

with K the undamaged material bulk modulus and G its undamaged shear modulus.

The time integration is realised thanks to an elastic predictor/plastic corrector algorithm (closest point algorithm)[1] in a time-step procedure where the stress tensor at time $n+1$ is computed from the stress tensor at time n in an iterative setup (Newton–Raphson algorithm).

The elastic predictor accounts only for the elastic strain rate and gives:

$$\begin{cases} \tilde{p}^e = \tilde{p}_n + K\,\mathrm{tr}\left(\Delta\boldsymbol{E}^N\right) \\ \tilde{\boldsymbol{s}}^e = \tilde{\boldsymbol{s}}_n + 2G\Delta\widehat{\boldsymbol{E}}^N \end{cases} \tag{19}$$

with $\Delta\widehat{\boldsymbol{E}}^N = \mathrm{dev}(\ln \boldsymbol{U})$ and $\mathrm{tr}\left(\Delta\boldsymbol{E}^N\right) = \mathrm{tr}(\ln \boldsymbol{U})$ for $\boldsymbol{U}$ the right stretch tensor evaluated between the configurations at time n and time $n+1$ (incremental strain resulting from the polar decomposition $\boldsymbol{F} = \boldsymbol{R}\boldsymbol{U}$ over the time step).

If needed (i.e. if $f = \tilde{\sigma}_{eq}^{vM} - \sigma_y > 0$), a plastic correction is performed for the deviatoric stress so that:

$$\tilde{\boldsymbol{s}}_{n+1} = \tilde{\boldsymbol{s}}^e - 2G\Gamma\boldsymbol{N}_{n+1} = \tilde{\boldsymbol{s}}^e - 2G\Gamma\frac{\mathbb{M} : \tilde{\boldsymbol{s}}_{n+1}}{\|\mathbb{M} : \tilde{\boldsymbol{s}}_{n+1}\|} \tag{20}$$

with $\Gamma = \int_{t_n}^{t_{n+1}} \Lambda\, dt$ and with the normal to the yield surface $\boldsymbol{N}$ computed at $n+1$ as a closest point projection scheme is used.

The internal variable driving the plastic problem is updated by:

$$\bar{\varepsilon}_{n+1}^{p,d} = \bar{\varepsilon}_n^{p,d} + \sqrt{\frac{2}{3}}\Gamma\frac{\|\tilde{\boldsymbol{s}}_{n+1}\|}{\|\mathbb{M} : \tilde{\boldsymbol{s}}_{n+1}\|} \tag{21}$$

where Γ is computed through a Newton–Raphson scheme to fulfil the yield criterion.

This procedure (Eqs. (20) and (21)) for computing $\tilde{\boldsymbol{s}}_{n+1}$ and Γ however results in a fully coupled non-linear system. The resolution of this system through a classical Newton–Raphson method unfortunately results in strong convergence problems. To overcome this, we can modify this system so that we get a linear system for the deviatoric stress integration. We can indeed choose to write the plastic strain rate in terms of a normal which is not a unit normal, such as $\boldsymbol{n}$ (Eq. (13)) instead of $\boldsymbol{N}$ (Eq. (11)):

$$\boldsymbol{D}^p = \lambda\boldsymbol{n} \tag{22}$$

We then have

$$\lambda = \frac{\Lambda}{\|\boldsymbol{n}\|} = \frac{\Lambda}{\|\mathbb{M} : \tilde{\boldsymbol{s}}\|} \tag{23}$$

Thus, the plastic correction (Eq. (20)) becomes:

$$\tilde{\boldsymbol{s}}^{n+1} = \tilde{\boldsymbol{s}}^e - 2G\gamma\mathbb{M} : \tilde{\boldsymbol{s}}^{n+1} \tag{24}$$

with $\gamma = \int_{t_n}^{t_{n+1}} \lambda\, dt$ the scalar plastic increment.

The plastic correction can thus be written in the form of a linear system in $\tilde{\boldsymbol{s}}_{n+1}$:

$$\mathbb{P} : \tilde{\boldsymbol{s}}_{n+1} = \tilde{\boldsymbol{s}}^e \tag{25}$$

where $\mathbb{P} = \boldsymbol{I}\underline{\otimes}\boldsymbol{I} + 2G\gamma\mathbb{M}$.

The internal variable driving the plastic problem is then computed as:

$$\bar{\varepsilon}_{n+1}^{p,d} = \bar{\varepsilon}_n^{p,d} + \sqrt{\frac{2}{3}}\gamma\|\tilde{\boldsymbol{s}}_{n+1}\| \tag{26}$$

To solve the plasticity problem, γ has to be computed so that $f = \tilde{\sigma}_{eq}^{vM}(\tilde{\boldsymbol{s}}) - \sigma_y(\bar{\varepsilon}^{p,d}) = 0$.

Starting with γ^0 as the value of the plastic multiplier at the end of the previous time-step, γ^i at the ith iteration of the Newton–Raphson algorithm is given by:

$$\begin{cases} \gamma^{i+1} = \gamma^i + \Delta\gamma \\ r^i = \tilde{\sigma}_{eq}^{vM}(\gamma^i) - \sigma_y(\gamma^i) \\ \Delta\gamma = -\dfrac{r^i}{\left.\frac{\partial\tilde{\sigma}_{eq}^{vM}}{\partial\gamma}\right|_{\gamma=\gamma^i} - \left.\frac{\partial\sigma_y}{\partial\gamma}\right|_{\gamma=\gamma^i}} \end{cases} \tag{27}$$

[1] During the elastic predictor step, $\boldsymbol{D} = \boldsymbol{D}^e$ and $\boldsymbol{D}^p = 0$ while for the plastic correction (if needed, i.e. if the elastic predictor does not satisfy the yield criterion) $\boldsymbol{D} = 0$ and $\boldsymbol{D}^p = \Lambda\boldsymbol{N}$.

The value of γ is iterated on until $\frac{r^{i+1}}{\sigma_y(\gamma^{i+1})} < TOL_\gamma$ with TOL_γ a user-chosen tolerance (chosen by default as 10^{-7}).

Details on the way to solve the deviatoric stress (Eq. (25)) and to compute the yield criterion derivative with respect to γ (Eq. (27)) are given in Appendix B.

The coupled problem (plasticity/anisotropic damage) has to be completed by an evolution law for the damage tensor. A priori, any thermodynamically consistent damage evolution could be used with this anisotropic damage elasto-plastic model. Compared to other integration algorithms used for anisotropic damage coupled to elastoplasticity (Lemaitre and Desmorat, 2005; Borgqvist and Wallin, 2013; El khaoulani and Bouchard, 2013; Brünig et al., 2008; Menzel and Steinmann, 2001; Abu Al-Rub and Voyiadjis, 2003), this staggered procedure has the advantage that it makes no assumption on the damage evolution other than keeping a symmetric damage tensor. It can thus be used for different materials having different damage mechanisms. It also leads to the derivation of a generic closed-form expression of the consistent tangent operator that can be applied to any damage evolution or isotropic hardening models provided they fit into the expression given in Eq. (15). The derivation of this operator is detailed in Appendix C. It is however restricted to a material whose undamaged behaviour can be modelled with a von-Mises elasto-plastic model and isotropic hardening. The same principle of integration can be used with other plastic criteria if the plastic update can be written as the canonical expression Eq. (25). Kinematic hardening can be considered if the corresponding terms of the consistent tangent operator are adapted. Finally, this staggered algorithm decouples the fully coupled non-linear system with 13 scalar unknowns into two smaller quasi linear systems: one of 7 scalar unknowns for the plasticity problem, non-linear in only the plastic multiplier, and one of 6 scalar unknowns, the anisotropic linear damage problem. On a computational point of view, it is thus obvious that the decoupled system requires less operations at each iteration for its resolution than the fully coupled one. Considering isotropic damage, it has been shown (Jeunechamps and Ponthot, 2013) that the staggered algorithm is indeed more efficient with respect to the CPU cost.

Two examples of completely different background are detailed in the next sections.

All numerical developments described have been implemented into the non-linear implicit object-oriented finite element code Metafor (developed at the LTAS/MN^{2}L, University of Liège, Belgium – www.metafor.ltas.ulg.ac.be) used in this work.

3. Application to ductile damage as a verification process

The modelisation of damage processes in ductile failure has been widely covered in the literature (Bonora et al., 2006; Brünig and Gerke, 2011; Luo et al., 2012; Mahnken, 2002; Shojaei et al., 2013). Recent reviews of models of ductile failure can be found in Besson (2010), Horstemeyer and Bammann (2010), Jeunechamps and Ponthot (2013) and references therein. Using a phenomenological approach of damage rather than a more physically motivated model has been regularly discussed and is judged controversial (Besson, 2009). The aim of this section however is neither to propose a new model of ductile failure nor to simulate an actual process but rather to demonstrate the versatility of the integration process presented in this work and to verify its implementation. For this purpose, the results of the simple uniaxial test of a ductile metallic matrix of a composite material proposed in Aboudi (2011) are reproduced. This matrix is made of a 2024-T4 aluminium alloy and its mechanical behaviour at constant temperature can be modelled using the approach presented in this work. All material parameters needed to model the elasto-plastic behaviour are described in Table 1. In his work, Aboudi (2011) uses the anisotropic damage evolution model of Lemaitre et al. (2000) as the aluminium alloy used is one of the material against which Lemaitre et al.'s (2000) model has been validated in the case of uncoupled plasticity. This model is a direct extension of the original isotropic Lemaitre's (1992) model and assumes the damage evolution is led by the plastic strain rate. It was initially built and used in an infinitesimal strain framework and is here extended to a finite strain formalism. The damage tensor evolution derived from a damage dissipation potential is written as:

$$\dot{\boldsymbol{d}} = \left(\frac{\tilde{Y}}{S}\right)^s |\boldsymbol{D}^p| \quad \text{if } \bar{\varepsilon}^p \geqslant \varepsilon_{th} \tag{28}$$

where S, s and ε_{th} are material parameters, the latter allowing for the damage to exist only above a threshold given in terms of the accumulated plastic strain and $\tilde{Y}$ is the effective elastic strain energy expressed in terms of the triaxiality function as:

$$\tilde{Y} = \frac{\tilde{\sigma}_{eq}^{vM\,2}}{2E} \underbrace{\left(\frac{2}{3}(1+\nu) + 3(1-2\nu)\left(\frac{\tilde{p}}{\tilde{\sigma}_{eq}^{vM}}\right)^2\right)}_{\text{triaxiality function}} \tag{29}$$

The principal directions of the damage rate are thus aligned with those of the plastic strain rate.

All material parameters needed to model the anisotropic damage are described in Table 2.

The problem studied in Aboudi (2011) and reproduced here is a uniaxial loading/unloading cycle up to 2% natural strain of a single hexahedral finite element. In this study a 8 nodes selectively reduced integration element (constant volumetric

Table 1
Material parameters of the 2024-T4 aluminium alloy at 21°C (Aboudi, 2011).

Young's modulus (GPa)	Poisson's ratio (–)	Yield stress (MPa)	Hardening coefficient (GPa)
72.4	0.33	286.7	11.7

Table 2
Damage parameters for the 2024-T4 aluminium alloy (Aboudi, 2011).

S (MPa)	s (–)	ε_{th} (–)	η (–)
0.05	1	0	2.6

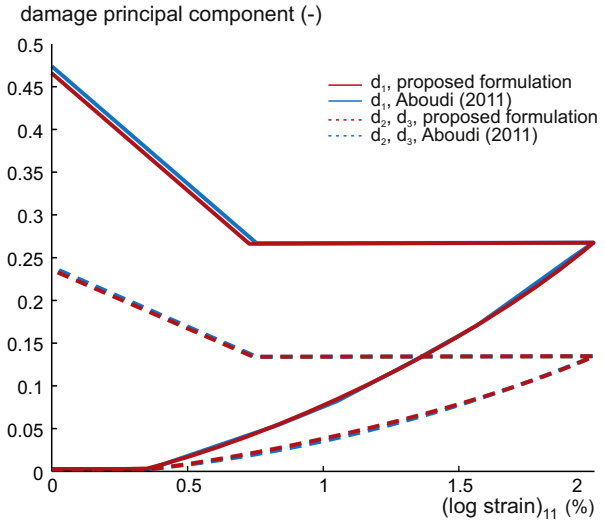

Fig. 2. Damage eigenvalues vs. natural strain for a loading–unloading uniaxial test.

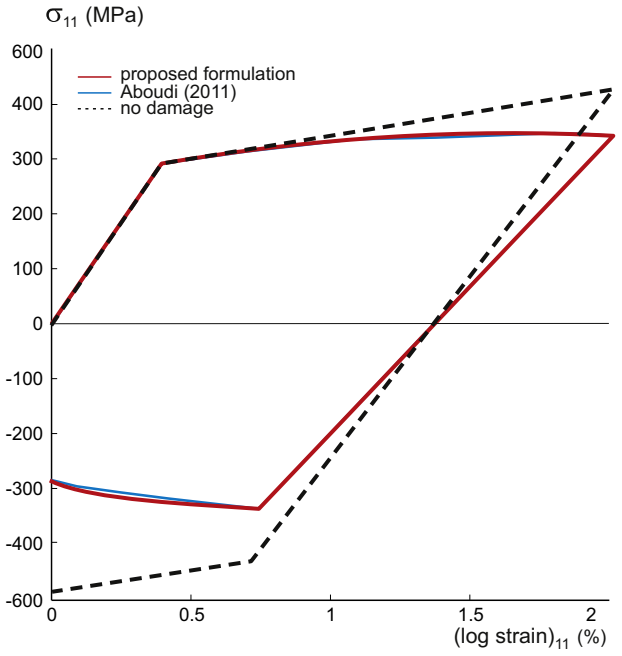

Fig. 3. Cauchy stress vs. natural strain for a loading–unloading uniaxial test.

strain) is used. Results of the damage eigenvalues evolution and the Cauchy stress are represented in Figs. 2 and 3 and compared to the results in Aboudi (2011). Fig. 2 shows the damage tensor rate induces anisotropy. Indeed, the damage eigenvalue $\boldsymbol{d}_1$ increases twice as much as the two other eigenvalues, proportionally to the plastic strain eigenvalues. The stiffness in the corresponding directions is inversely proportional to the damage eigenvalues, thus producing a transversely isotropic stiffness. A difference below 0.5% is observed between the results obtained with the present approach and the results of Aboudi (2011). This difference can be explained by the way the numerical algorithm to integrate the constitutive law is considered converged. Indeed, the approach of de Souza Neto et al. (2011) used by Aboudi (2011) evaluates the

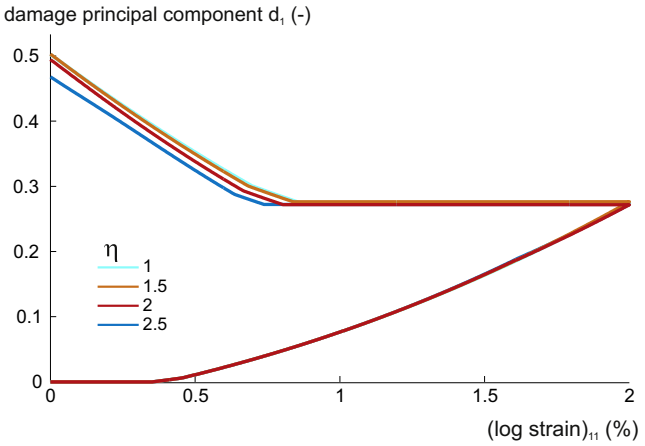

Fig. 4. Damage eigenvalue vs. natural strain for a loading–unloading uniaxial test and different values of η.

convergence over the whole coupled system including plastic strain increment and damage tensor, $\boldsymbol{d}$. However, in the present approach, the constitutive law is considered as converged when the increment of the effective damage tensor, $\boldsymbol{H}$, is stationary. Fig. 3 shows the effect damage has on the material. The material hardening is reduced by comparison to the undamaged state in the loading case. The unloading has a lower slope than the loading one as the damage effect on the elastic stiffness has a softening effect. Finally the damage effect on the plastic unloading is a softening effect while the undamaged material still follows a hardening law.

Fig. 4 shows the effect the hydrostatic parameter η has on the damage evolution. The end value of the damage eigenvalues decreases within increasing η. This effect of η depends however on the triaxiality as it weights the hydrostatic and deviatoric part of the damage rate. Here as only a uniaxial test is performed, the triaxiality function is constant. For a variable triaxiality, the effect of η is not however as simple as observed in the present case.

This simple example showed the damage integration approach presented in this work produces similar results when compared to more computationally expensive coupled approaches such as the integration scheme of de Souza Neto et al. (2011). It also showed a simple extension of the original Lemaitre damage rate to anisotropy is sufficient to imply large orthotropic effects in the material. Finally, the effect of damage on the elastic part of the deformation is clearly highlighted in a loading/unloading cycle as the unloading elastic slope is lower than the loading one.

4. Damage-like biological application: a model for orthodontic tooth movement

This section aims at proposing a biomechanical application of the anisotropic damage framework presented. This framework has already been applied to bone (Zysset and Curnier, 1996; Garcia et al., 2009), articular cartilage (Hosseini et al., 2014), intervertebral disc (Qasim et al., 2014), and other soft tissues (Bernick et al., 2011; Balzani et al., 2012; Calvo et al., 2009). In this work, an orthodontic tooth movement model is developed and applied to two representative types of tooth movements.

4.1. Generic principles of orthodontics and bone remodelling

The basic principle in orthodontics is to gradually impose progressive and irreversible bone deformations using specific force systems on the teeth. In orthodontic treatments, the tooth displacement is mainly due to bone remodelling that leads the teeth into new positions (Krishnan and Davidovitch, 2009; Masella and Chung, 2008; Lindauer, 2001; Melsen, 2001). Both cortical an cancellous bone (see Fig. 5), as adapted, adjustable, and optimised living structures, are constantly renewed. This permanent remodelling is an adaptive process that beyond biological aspects depends on the mechanical loading on the skeleton. It aims at preserving the mechanical properties of the bone and adapting its structure in response to the mechanical demands it experiences. It decreases the amount of bone where it is of no mechanical relevance; while it increases its density to reinforce bone where it is necessary. Besides the density change, remodelling also occurs to modify the bone topology, mainly in trabecular bone tissue for which the trabeculae tend to align along the principal stress directions. Bone remodelling therefore depends not only on the load intensity but also on the load directions.

From a phenomenological point of view and as explained by the mechanostat theory (Frost, 1964, 1987), remodelling occurs in order to homogenize at the tissue level a stimulus, ψ_t, in the neighbourhood of an homeostatic tissue level value, $\psi_t^\star$. This stimulus is a scalar representation of the applied mechanical loads. Remodelling can be modelled by relating the bone density rate, $\dot{\rho}$, to a remodelling rate, $\dot{r}$ (Beaupré et al., 1990).

$$\dot{\rho} = kS_v\rho_0\dot{r} \tag{30}$$

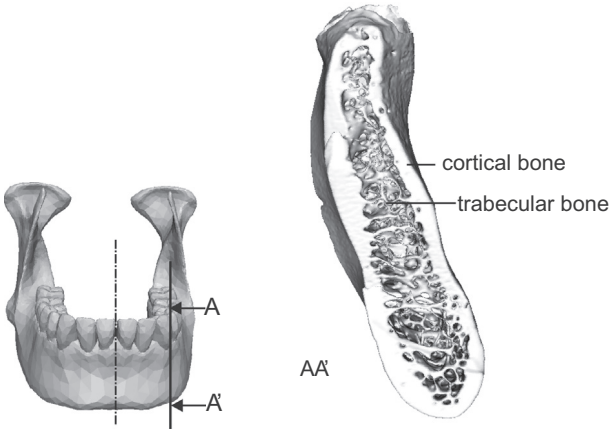

Fig. 5. Alveolar bone of a mandibular left canine (79-year-old male). Trabecular (or cancellous) internal structure and cortical shell (stl file from Boryor et al. (2009)).

with ρ the apparent density and ρ_0 the density of the fully mineralised bone tissue. The terms kS_v in Eq. (30) take into account the available ($k \in [0,1]$) bone specific surface area (S_v internal surface area per unit volume). They thus express the fact that a bone surface has to exist for bone cells to act and induce remodelling. k accounts for the fact that all this surface is not available for the cells to act. The specific surface area S_v can be related to the porosity $f = 1 - \frac{\rho}{\rho_0}$.

The remodelling rate $\dot{r}$ is a function of the difference between the current value of the chosen stimulus, ψ_t, and its homeostatic counterpart, $\psi_t^\star$. For anisotropic models, the change in trabecular orientation is modelled through a change of the stiffness directionality related to the external loads direction. Most models also assume the existence of a "dead" or lazy zone (an interval, of half-width ω, around the homeostatic level for which no remodelling process takes place). The remodelling rate needs to be defined is such a way that remodelling takes place to resorb bone ($\dot{r} < 0$) and decrease the apparent density where "underloaded" conditions are encountered, $\psi_t < \psi_t^\star - \omega$, while formation of bone ($\dot{r} > 0$) occurs (increase of density) where "overloaded" conditions are encountered, $\psi_t > \psi_t^\star + \omega$. These conditions for remodelling are usually called the remodelling criteria and are sketched in Fig. 6.

The original model which is proposed in this work is built on a damage/repair based approach of remodelling. It is a phenomenological model, stated first by Doblaré and co-workers (Doblaré and García, 2002; García et al., 2002). This model has been chosen as a framework because it is one of the few models whose stimulus variation is justified through thermodynamical concepts of Continuum Mechanics. It is also one of the few models for which the remodelling law is fully integrated into the constitutive model. In the case of bone remodelling, "damage" has to be understood as a measure of the bone topology (bone density and trabecular orientation). The measure of damage used is therefore virtual and actually reflects the bone density and orientation that can evolve. There is no actual damage in the tissue. The undamaged material is the ideal situation of bone with null porosity and perfect isotropy, i.e. the material considered for the fully mineralised bone. The process of bone resorption corresponds to the classical damage evolution concept, since it increases the void fraction and therefore damage. However, bone apposition can reduce damage and lead to bone repair. Damage repair can be considered because the total energy dissipation also includes biological dissipation due to metabolism on top of the mechanical dissipation which is negative for damage repair (Jacobs, 1994).

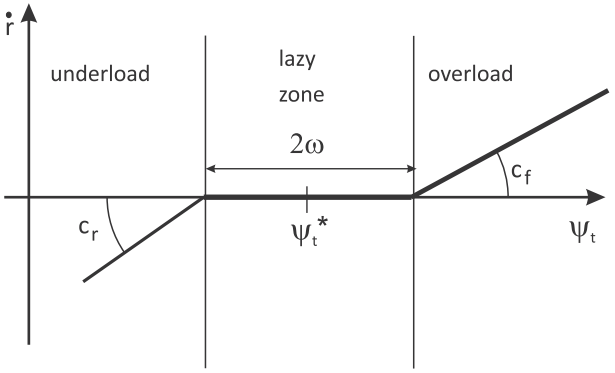

Fig. 6. Remodelling rate as a function of the remodelling stimulus.

In the present work, Doblaré and García (2002) and García et al.'s (2002) model is firstly enhanced to be coupled to an elasto-plastic material behaviour in a finite strain framework (see Mengoni and Ponthot (2010) for an isotropic version of this elasto-plastic damage coupling). The new model can therefore capture permanent strains of the tissue beyond the ones due to the density variation only. The bone tissue topology is here considered as an anisotropic "organization" of elasto-plastic trabeculae (although it is clear that the relevant inelastic process is different from that of the classical metal plasticity). This "organization" is measured through morphological parameters: a mean bone density, or bone volume fraction i.e. bone volume over total volume: $\mathtt{BV/TV}$ or $\bar{\rho} = \rho/\rho_0$, and a fabric tensor ($\boldsymbol{T}$ as defined in Cowin (1986)) that measures of the amount of bone tissue in a given direction and describes the anisotropy. The plastic behaviour may not be relevant in bone remodelling applications due to the very low strain levels involved, permanent strains due to density variations are much higher than the one due to a plastic behaviour. However, the proposed model can be used both in low strain levels and higher strain levels problems keeping the continuum representation of the topology through the use of the fabric tensor and allowing to represent a plastic behaviour of the bone trabeculae.

The remodelling model is secondly slightly modified to account for complex biological behaviour of the periodontal ligament, i.e. the soft tissue membrane laying between the tooth and its supporting alveolar bone (see Section 4.3).

Even tough it was not the approach followed here, it should be noted that Voyiadjis and Kattan (2006) proposed generic anisotropic damage models related to the morphology through the use of fabric tensors. They used fourth order damage tensors, related to a fabric tensor representing crack distributions. Their aim was to provide a sound physical meaning to an anisotropic representation of damage in elastic theories.

4.2. Phenomenological remodelling model expressed in the continuum damage theory framework

To apply Doblaré and García (2002) and García et al.'s (2002) model within the theoretical framework presented earlier, the effective stress definition is represented in a strain equivalence approach of damage. The yield criterion is expressed for the undamaged material, here the fully mineralised bone. Actually, this anisotropic model is applied to trabecular bone only while the cortical bone is considered as initially isotropic and remaining isotropic during remodelling, thus following an isotropic version of this anisotropic model (Mengoni and Ponthot, 2010).

We thus define an anisotropic damage tensor that depends on morphological parameters ($\mathtt{BV/TV}$ or $\bar{\rho}$ and fabric tensor: $\boldsymbol{T}$) by the expression:

$$\boldsymbol{d} = \boldsymbol{I} - \bar{\rho}^{\beta} A \boldsymbol{T} \tag{31}$$

where A is a calibration functions that allows to retrieve the classical formulation of damage in the isotropic case, and β is the exponent of the power law relating $\bar{\rho}$ to the bone Young's modulus, E (β can be function of $\bar{\rho}$), i.e. $E \propto \bar{\rho}^{\beta}$ (Jacobs, 1994).

This definition of damage fulfils the requirements of a damage variable, i.e. $\boldsymbol{d} = \boldsymbol{0}$ for $\bar{\rho} = 1$ and $\boldsymbol{T} = \boldsymbol{I}$ (pure isotropy), corresponding to the undamaged state, and $\boldsymbol{d} = \boldsymbol{I}$ for $\bar{\rho} = 0$ and any value of $\boldsymbol{T}$; which means complete absence of bone mass. Using a normalisation condition for $\boldsymbol{T}$, such as $\mathtt{tr}(\boldsymbol{T}) = 3$, yields to the independence of the two internal variables, $\boldsymbol{d}$ and $\bar{\rho}$ (Doblaré and García, 2002).

Considering Eqs. (4) and (31), we see that the effective damage tensor $\boldsymbol{H}$ has its principal directions aligned with the fabric tensor $\boldsymbol{T}$ principal directions:

$$\boldsymbol{H}^{-2} = \bar{\rho}^{\beta} A \boldsymbol{T}$$

This effective damage tensor includes not only the directionality of the bone microstructure through the fabric tensor ($\boldsymbol{T}$), but also the porosity by means of the density ($\bar{\rho}$). A remodelling law affecting both $\bar{\rho}$ and $\boldsymbol{T}$ will thus be translated into a damage evolution law.

In order to derive an evolution law for the effective damage tensor $\boldsymbol{H}$, or equivalently for the fabric tensor $\boldsymbol{T}$, we define an external mechanical stimulus, $\boldsymbol{Y}$, identified as the variable thermodynamically conjugated to the effective damage tensor in terms of the free energy density function (Ψ).

$$\boldsymbol{Y} = -\frac{\partial \Psi(\boldsymbol{\sigma}, \boldsymbol{H})}{\partial \boldsymbol{H}} \tag{32}$$

This free energy density is calculated considering an isotropic material behaviour at trabecular level (and assuming we can extend the expression of the free energy density in small strains to a finite strain problem) and expressing it in terms of Cauchy stress as:

$$\Psi = \frac{1}{2}\left(\frac{p^2}{K(1-\eta d^H)} + \frac{1}{2G}\mathtt{tr}(\boldsymbol{H}\,\boldsymbol{s}\,\boldsymbol{H}\,\boldsymbol{s})\right) \tag{33}$$

$\boldsymbol{Y}$ is then obtained in terms of the external independent variable (Cauchy stress, $p, \boldsymbol{s}$) and the internal variable (effective damage tensor, $\boldsymbol{H}$) as (deriving Eq. (33) with respect to $\boldsymbol{H}$):

$$\boldsymbol{Y} = \frac{1}{3K}\frac{\eta p^2}{(1-\eta d^H)^2}\boldsymbol{H}^{-3} + \frac{1}{2G}\boldsymbol{s}\,\boldsymbol{H}\,\boldsymbol{s} \tag{34}$$

The damage criterion is the domain of the external mechanical stimulus, $\boldsymbol{Y}$, for which damage is not modified (the lazy zone as used in the literature of bone remodelling) both in overload and underload conditions. Following Doblaré and García (2002) and García et al.'s (2002) approach and adapting it to the present formalism, we propose two damage criteria, g_o and g_u, one for overloaded conditions and one for underloaded ones:

$$\text{Overload}: \quad g_o = C\frac{3^{1/4}}{\sqrt{1-w}}(\boldsymbol{J}:\boldsymbol{J})^{1/4} - (\psi_t^\star + \omega)\rho^{2-\beta/2} \tag{35}$$

$$\text{Underload}: \quad g_u = -C\frac{3^{1/4}}{\sqrt{1-w}}(\boldsymbol{J}:\boldsymbol{J})^{1/4} + (\psi_t^\star - \omega)\rho^{2-\beta/2} \tag{36}$$

with $\boldsymbol{J} = \mathbb{W}:\boldsymbol{Y} = \frac{1}{3}(1-2w)\mathrm{tr}(\boldsymbol{Y})\boldsymbol{I} + w\boldsymbol{Y}$.

Considering an associated evolution law for the effective damage tensor, we can write:

$$\dot{\boldsymbol{H}} = \mu^o\frac{\partial g_o}{\partial \boldsymbol{Y}} + \mu^u\frac{\partial g_u}{\partial \boldsymbol{Y}} \tag{37}$$

where μ^o and μ^u are flow parameters with the consistency conditions $\mu^o, \mu^u \geqslant 0;\ g_o, g_u \leq 0;\ \mu^o g_o = \mu^u g_u = 0$.

Deriving the remodelling criteria (Eqs. (35) and (36)), combining with the effective damage tensor definition (Eq. (4)), and the density variation (Eq. (30)), the evolution law of the effective damage tensor becomes for both underload and overload conditions:

$$\dot{\boldsymbol{H}} = -\frac{\beta k S_v \dot{r}}{2}\frac{\mathrm{tr}\left(\boldsymbol{H}^{-2}\right)}{\mathrm{tr}\left(\boldsymbol{H}^{-3}(\mathbb{W}:\boldsymbol{J})\right)}\frac{\rho_0}{\rho}\mathbb{W}:\boldsymbol{J} \tag{38}$$

As two parameters, w in the definition of $\mathbb{W}$, and η in the definition of $\tilde{\boldsymbol{\sigma}}$, are defined to weigh the deviatoric and hydrostatic parts of tensors, and as they are defined on two distinct intervals ($w \in [0,1[$ and $\eta \in [1,+\infty[$), we actually use $w = 1 - e^{-(\eta-1)}$ to reduce the number of parameters to one. This (w,η) mapping is a continuous mapping between a parameter, η, defined in an infinite interval and one, w, defined in a finite interval. As η is usually bounded (about 3 for metals (Lemaitre and Desmorat, 2005) and taken to be equal to the degree of anisotropy in the case of bone), the choice of this relationship induces no numerical difficulties (while w would tend to 1 for large values of η and the division by $(1-w)$ in Eqs. (35) and (36) would not be possible otherwise).

The remodelling rate $\dot{r}$ is obtained from the remodelling criterion that is currently active (see Fig. 6):

$$\dot{r} = \begin{cases} -c_r\frac{g_u}{\rho^{2-\beta/2}} & \text{for } g_u \geqslant 0,\ g_o < 0, \\ 0 & \text{for } g_u < 0,\ g_o < 0, \\ c_f\frac{g_o}{\rho^{2-\beta/2}} & \text{for } g_o \geqslant 0,\ g_u < 0, \end{cases} \tag{39}$$

The parameters c_r and c_f are related to the remodelling velocity. They are usually chosen as constant such as in Fig. 6. They can however generally be function of the remodelling stimulus or another measure of stress.

Finally, the density variation can be computed from Eq. (30). It has to be emphasised however that this density change is not actually used to compute a change of mass. Only the stiffness variation due the density rate is used as the density is considered having an influence on stiffness only. Therefore, there is no actual change of mass considered in the bone. The terms formation and resorption are thus employed as increase and decrease of stiffness respectively.

4.3. Application to orthodontic tooth movement

Such a remodelling model cannot be used straight away in an orthodontic tooth movement problem. Indeed in this case, the remodelling is driven not only by the bone cells reactions to the applied loads but also by the periodontal ligament's cells (Krishnan and Davidovitch, 2009; Masella and Chung, 2008; Lindauer, 2001). The periodontal ligament is the soft membrane laying between the bone and the teeth. Its role is not only to be a buffer membrane between two hard tissues but also to provide a blood flow to these tissues (Melsen, 2001; Verna et al., 2004), blood flow which is necessary for the bone cells to induce remodelling. When forces are applied to the tooth by orthodontic devices, the blood flow within the ligament is disrupted and so is the cell activity. This change of cell activity (mainly the fibroblasts) triggers remodelling, which is thus strongly related to the hydrostatic pressure (Van Schepdael et al., 2013). In such a situation, bone resorption will be observed for underload situations and overload situations in compression while bone formation will arise in overload situations in tension only. In order to account for this difference in the model, a slight change is made in the definition of the remodelling rate. Instead of using a remodelling rate such as defined in Eq. (39) with a constant remodelling coefficient c_f in overloaded situations, we define a piecewise constant remodelling coefficient in overloaded situations that accounts for all phenomenon in the periodontal ligament. This coefficient c depends on the hydrostatic stress in such a way that it is positive in tension, negative in compression, and null for high compression situations where the blood and cell flow is completely interrupted (Fig. 7).

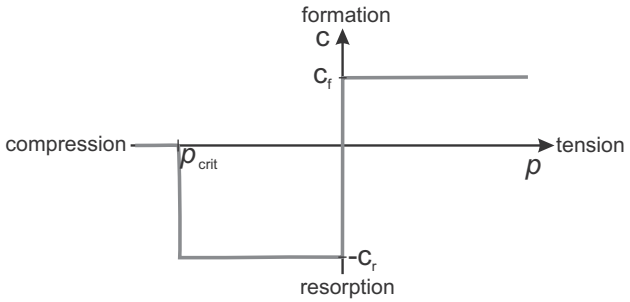

Fig. 7. Value of the remodelling coefficient c as a function of the hydrostatic pressure for the remodelling law adapted to the specific case of orthodontic tooth movement in overloaded conditions.

This model (anisotropic remodelling adapted to orthodontic problem and expressed in a Continuum Damage framework) is here applied to a characteristic situation in orthodontics, a tooth translation (bodily tooth movement in 2D and intrusion in 3D) into its supporting bone (see Fig. 8). The bodily tooth movement is modelled as an applied displacement in the case of a 2D analysis. The intrusion is due to an applied force in a 3D analysis. In both cases, the tooth is considered rigid, the periodontal ligament mechanical behaviour follows a non-linear interface model (Mengoni, 2012), and the bone follows mechanical and remodelling laws such as described in this work. Both trabecular and cortical bone are initially isotropic. Trabecular bone can evolve to become anisotropic while it is assumed that cortical bone remains isotropic. The consideration of a von-Mises plasticity for the trabecular level has been discussed previously (Bayraktar and Keaveny, 2004; Mengoni et al., 2012; Verhulp et al., 2008) and is considered here as a valid assumption. Such a criterion homogenised with a fabric tensor leads to an apparent level plastic criterion that can be characterised as a general Hill criterion in the orthotropy axis defined by the fabric tensor (Mengoni, 2012). All material and remodelling parameters of the modelled tissues are described in Table 3. In particular, at tissue level, the yield limit is chosen to be 200 MPa (median value of the one calculated with a reverse engineering approach on linear finite element models in Niebur et al. (2000), Stölken and Kinney (2003) and Verhulp et al. (2008)). The isotropic hardening parameter is computed so that the tangential modulus is set to 5% of the value of Young's modulus as in the previously cited studies. The remodelling parameters are not particularised to orthodontic models and are those of Doblaré and García (2002). However, given that for the initial state, for which there is equilibrium, $\psi = 0$ and that only orthodontic loads are considered, the reference stimulus, $\psi^\star$, is here taken at zero also. A more realistic model accounting for all forces (i.e.; muscle tone, chewing forces, mouth activity, gravity) and a non-zero stimulus at equilibrium would lead to a better choice of reference stimulus. This choice of reference stimulus will in particular not allow modelling the loss of bone following a tooth loss. It indeed does not account for possible loss of stiffness due to underuse.

The tissues geometries were extracted from CT-scans images (obtained from the OSIRIX image dataset[2]). These CT images of a mandible were segmented into cortical bone, trabecular bone, and teeth (see Fig. 8). For the 2D analysis (plane strain), a slice of the left central incisor in the mesiodistal plane was extracted and a geometry using cubic splines for the tooth, trabecular bone, and cortical bone was built. This geometry was then meshed with linear quadrilaterals with constant pressure. For the 3D analysis, a multiple material surface mesh was constructed (d'Otreppe et al., 2012), and a volumic mesh built using linear tetrahedra.

4.3.1. Bodily tooth movement

The 2D problem is a displacement driven problem. The tooth is translated perpendicularly to its main axis (see Fig. 8) over a distance corresponding to the periodontal ligament width and kept at that position over a period of six months. The effect of remodelling can be observed globally by a decrease of the force needed to sustain such a displacement and locally by a density and orientation change within the bone. Bone density variation is observed during this constant displacement period, leading to a reduction of the needed force as depicted in Fig. 9 (plain curve). The initial force intensity needed to move the tooth is 1.24N, i.e. a value that can be compared to clinically applied forces (Roberts, 2000; Bourauel et al., 2000). This initial force causes high hydrostatic stress in the compression side, impeaching remodelling to occur as c (Fig. 7) is zero. Thus initially only bone formation can occur in the tension side of the tooth (right in the figure), increasing the needed force to maintain the displacement. On the compression side, peripheral (with respect to the bone/tooth interface) remodelling slowly decreases the density (see Fig. 10, left) and thus the compressive hydrostatic stress. The force needed to maintain the displacement then decreases due to direct remodelling once the hydrostatic stress at the compression side has been reduced (after about forty days see Fig. 10, right). A force reduction by a factor of two is observed in the following 20 days. After 150 days of remodelling, the force has been reduced by six and stabilizes at that asymptotic level further on. We can also notice that after 70 days (Fig. 10, right zoomed area), the contours of the bone at the bone/tooth interface matches those of the tooth, as remodelling tends for the bone to follow the tooth. This was obviously not yet the case after 35 days (Fig. 10,

[2] OSIRIX/INCISIX dataset http://www.osirix-viewer.com/datasets/.

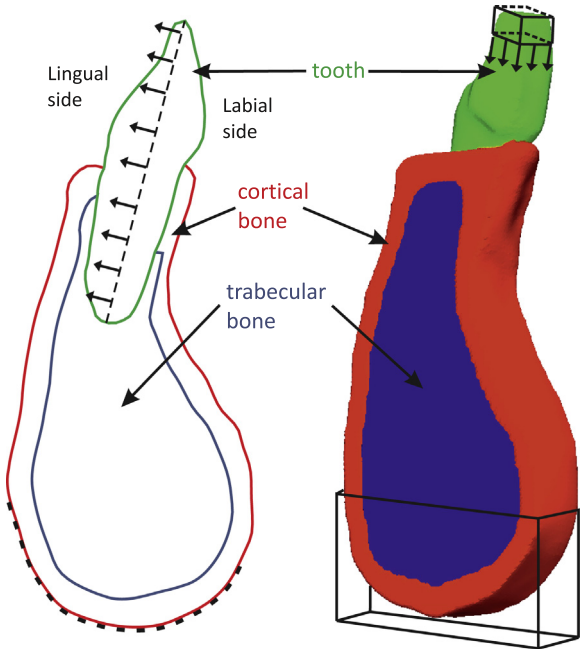

Fig. 8. Geometries and boundary conditions of the orthodontic tooth movement models. Left: 2D incisive submitted to bodily tooth movement, the bottom dashed curve is constrained. Right: 3D incisive submitted to an intrusion movement, the surface within the bottom box is constrained.

Table 3
Material and remodelling parameters of bone tissues.

Remodelling parameters				
$\psi^\star$ (MPa)	c_r (μm/(day MPa))	c_f (μm/(day MPa))	ω (MPa)	η (–)
0	10	5	0.1	1

Mechanical parameters					
Material	Young's modulus (GPa)	Poisson's ratio (–)	Yield stress (MPa)	Hardening parameter (MPa)	Apparent density (gr/cc)
Bone at tissue level	13.75	0.3	200.0	723.7	
Trabecular bone					0.95
Cortical bone					1.805

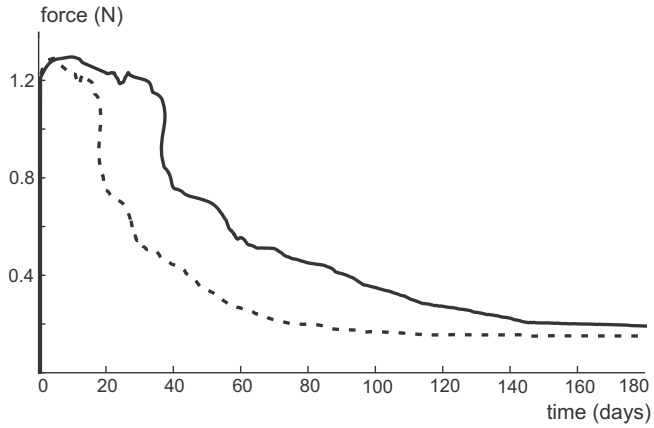

Fig. 9. Displacement driven tooth movement – intensity of the force (N) needed to maintain a displacement over time (days). Plain curve: translation movement, and dashed curve: translation with a remodelling constant twice as high as the previous one.

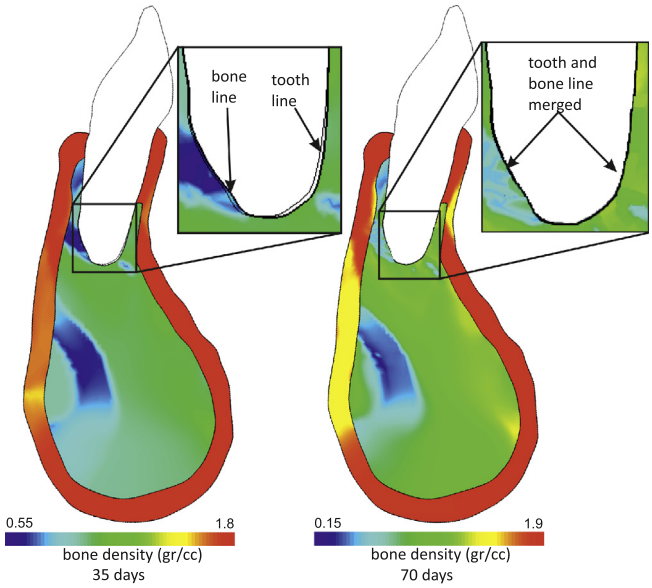

Fig. 10. Displacement driven tooth movement – bone density [gr/cc] after 35 days (left) and after 70 days (right). Initial values for trabecular bone: 0.95 gr/cc, for cortical bone: 1.805 gr/cc

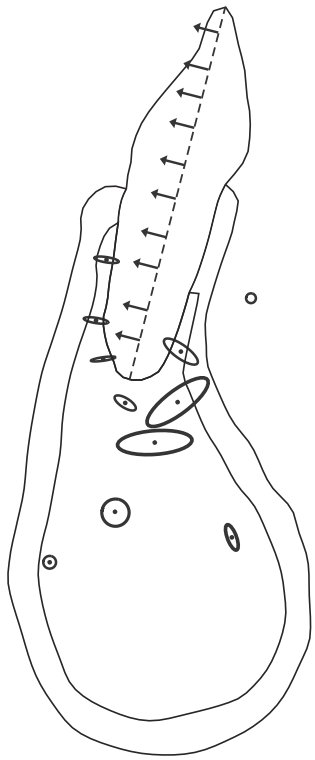

Fig. 11. Trabecular bone orientation – movement of translation after 180 days. The ellipses represent the stiffness eigenvalue (the axis orientations are those of the fabric tensor eigenvectors and their lengths are proportional to the fabric tensor eigenvalues), a 1 GPa isotropic indicator is also depicted on the right side of the tooth.

left zoomed area) where a space between tooth and bone exists representing the stretching or compression of the periodontal ligament due to mechanical loading. After a certain amount of time, this altered situation of the periodontal ligament is eliminated thanks to the bone remodelling process. If the same model is considered with a faster remodelling (e.g. doubling

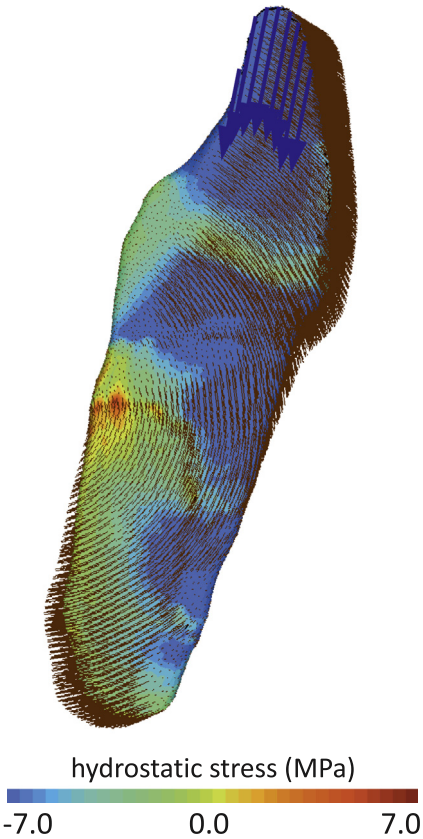

Fig. 12. Intrusion: hydrostatic stress (MPa, positive in tension) after a month of remodelling. The blue arrows represent the application of the intrusion force. The brown lines represent the displacement field, enhancing the rotation behaviour. (For interpretation of the references to color in this figure legend, the reader is referred to the web version of this article.)

the remodelling constants c_f and c_r), the behaviour is identical to the previously described but with a twice as fast response (Fig. 9, dashed curve). Those constants are indeed the only drivers of time in the model of remodelling developed in this work. Fig. 10 also shows a ring shape area (in blue[3]) on the lower left side of the trabecular bone where high resorption has occurred. The presence of this area is only a numerical boundary condition artefact. As its effect does not extend to the base of the tooth root, it does not perturb the remodelling around the tooth.

The remodelling also has an effect on the trabecular orientation in the bone. This effect can be assessed by analysing the stiffness eigenvalues and eigenvectors that represent the principal directions. As seen in Fig. 11, while the initial configuration was an isotropic bone, after 150 days it is completely different. The trabecular bone is highly oriented around the tooth to be stiffer in the direction of displacement while it remained almost unaffected in the basal bone.

4.3.2. Tooth intrusion

This 3D problem is a force driven problem. Due to applied forces, the tooth is intruded into the bone (see Fig. 8). This movement is obtained applying a $0.7N$ force on the tip of the crown, towards the apex of the tooth (the force is applied with a constant direction, whatever the tooth movement). The force is kept constant for three months while the bone density variation observed during this period leads to an increase of the tooth displacement.

The obtained displacement is directed towards the tooth apex, however due to the non-linearity of the periodontal ligament, it is composed of a translation and a slight rotation (see Fig. 12). The initial displacement of 0.18 mm (see Fig. 13) is due to the periodontal ligament deformation mainly. It creates high compression of the bone along most of the tooth/bone interface, thus impeaching direct remodelling. The remodelling thus takes initially place either away from the bone/tooth interface (peripheral resorption), or to form new bone. The first remodelling effect is thus a very low decrease of the displacement. As seen in Fig. 13, the displacement rate increases after about 15 days when direct remodelling is then possible. The tooth displacement (Fig. 13), while initially decreasing because of the bone formation apically, slowly increases to reach an increase of 50% of the initial (instantaneous) displacement.

[3] For interpretation of color in Fig. 10, the reader is referred to the web version of this article.

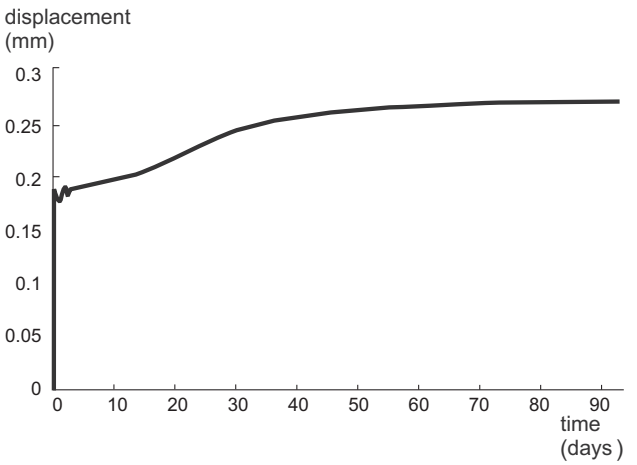

Fig. 13. Intrusion: displacement of the tooth (mm) vs. time (days).

5. Conclusions

This paper presented two main original contributions.

First, a numerical integration procedure for an anisotropic continuum damage model coupled to elasto-plasticity was proposed in a finite strain context. It is a staggered scheme of integration instead of a fully coupled integration procedure often found in the literature. This allowed us to reduce the computational cost of such an integration algorithm. Indeed the staggered scheme solves two decoupled systems of 7 scalar unknowns (for the plasticity problem, non-linear in only the plastic multiplier) and 6 scalar unknowns (the anisotropic linear damage problem) instead of a fully coupled non-linear system with 13 scalar unknowns. This integration scheme was verified against a simple uniaxial test from the literature. Moreover, the proposed algorithm allows exact linearisation, leading to the derivation of a generic closed-form expression of the consistent tangent operator. This quadratic rate of convergence of the full Newton–Raphson scheme is thus preserved.

Second, a constitutive model able to simulate the coupled biological and mechanical phenomenon within the bone in orthodontic tooth movement applications was developed. Compared to other tooth movement models of the literature, the remodelling behaviour is fully included into a non-linear constitutive law for the bone. This constitutive model is built on morphological parameters to describe the bone anisotropy, accounting for effects such as plasticity of the trabeculae, and for which the continuum parameters such as the stiffness can evolve with morphology as remodelling occurs in the tissue. In spite of the necessary idealizations, the proposed phenomenological description of bone remodelling specified for alveolar bone allows to qualitatively represent density variation of the bone surrounding a tooth when submitted to loading representative of orthodontic appliances. Simple cases of orthodontic tooth movements can be represented with the present model when applied to geometries reconstructed from CT-scans images. However the presented applications did not simulate the effect of actual orthodontic devices, in particular further work should focus on a more realistic representation of boundary and initial conditions. Indeed, we assumed that the only forces present during orthodontic tooth movement where the orthodontic forces, neglecting all physiological forces (muscle tone, chewing forces and other mouth activities, as well as gravitational forces). We thus used a value of the remodelling stimulus that was not physiological but was representative of the equilibrium state of the proposed computational approach. Moreover, it has been shown that remodelling algorithms such as the one used here exhibit a high sensitivity to boundary conditions. Obtaining a better computational representation of those conditions is thus a necessary step to produce predictive orthodontic tooth movement models.

The approach taken here in the development of the integration scheme was general and allowed for two completely different damage rates to be used (ductile damage and biomechanical tissue adaptation). Its implementation into an object-oriented finite element code facilitates the addition of any new damage models coupled to any new isotropic hardening laws.

Appendix A. Deriving the plastic flow rule for the anisotropic damage model

The plastic strain rate is assumed to follow the normality rule (associated plasticity) in the Cauchy stress space. For a von-Mises yield function, it gives:

$$\boldsymbol{D}^p = \Lambda \boldsymbol{N} = \Lambda \frac{\frac{\partial f(\tilde{\boldsymbol{s}})}{\partial \boldsymbol{\sigma}}}{\|\partial f / \partial \boldsymbol{\sigma}\|}$$

with $f = \tilde{\sigma}_{eq}^{vM} - \sigma_y$ and $\frac{\partial f(\tilde{\boldsymbol{s}})}{\partial \boldsymbol{\sigma}} = \frac{\partial f(\tilde{\boldsymbol{s}})}{\partial \tilde{\boldsymbol{s}}} \frac{\partial \tilde{\boldsymbol{s}}}{\partial \boldsymbol{\sigma}}$

$$\boldsymbol{D}^p = \Lambda \frac{\frac{\partial f(\tilde{\boldsymbol{s}})}{\partial \boldsymbol{\sigma}}}{\|\partial f/\partial \boldsymbol{\sigma}\|} = \Lambda \frac{\tilde{\boldsymbol{s}} : \frac{\partial \tilde{\boldsymbol{s}}}{\partial \boldsymbol{\sigma}}}{\left\|\tilde{\boldsymbol{s}} : \frac{\partial \tilde{\boldsymbol{s}}}{\partial \boldsymbol{\sigma}}\right\|} \tag{A.1}$$

Upon writing

$$\tilde{\boldsymbol{s}} = \mathtt{dev}(\boldsymbol{H}\,\boldsymbol{s}\,\boldsymbol{H}) = \boldsymbol{H}\,\boldsymbol{s}\,\boldsymbol{H} - \frac{1}{3}\mathtt{tr}(\boldsymbol{H}\,\boldsymbol{s}\,\boldsymbol{H})\boldsymbol{I} \tag{A.2}$$

one gets (assuming $\boldsymbol{H}$ constant[4])

$$\frac{\partial \tilde{s}_{ij}}{\partial \sigma_{kl}} = \frac{\partial H_{im} s_{mn} H_{nj}}{\partial \sigma_{kl}} - \frac{1}{3}\frac{\partial H_{qr} s_{rs} H_{sq}}{\partial \sigma_{kl}}\delta_{ij} = \left[H_{ik}H_{lj} - \frac{1}{3}H_{im}H_{mj}\delta_{kl}\right] - \frac{1}{3}\left[H_{qk}H_{lq} - \frac{1}{3}H_{qr}H_{rq}\delta_{kl}\right]\delta_{ij} \tag{A.3}$$

One can therefore write ($\tilde{\boldsymbol{s}}$ being deviatoric and $\boldsymbol{H}$ symmetric[5])

$$\tilde{s}_{ij}\frac{\partial \tilde{s}_{ij}}{\partial \sigma_{kl}} = \tilde{s}_{ij}\left[H_{ik}H_{lj} - \frac{1}{3}H_{im}H_{mj}\delta_{kl}\right] = H_{ki}\tilde{s}_{ij}H_{jl} - \frac{1}{3}H_{mi}\tilde{s}_{ij}H_{jm}\delta_{kl} \tag{A.4}$$

or equivalently

$$\tilde{\boldsymbol{s}} : \frac{\partial \tilde{\boldsymbol{s}}}{\partial \boldsymbol{\sigma}} = \mathtt{dev}(\boldsymbol{H}\,\tilde{\boldsymbol{s}}\,\boldsymbol{H}) \tag{A.5}$$

and eventually

$$\boldsymbol{D}^p = \Lambda \boldsymbol{N} = \Lambda \frac{\mathtt{dev}(\boldsymbol{H}\,\tilde{\boldsymbol{s}}\,\boldsymbol{H})}{\|\mathtt{dev}(\boldsymbol{H}\,\tilde{\boldsymbol{s}}\,\boldsymbol{H})\|} \tag{A.6}$$

The flow direction (unit normal to the yield function) is given by

$$\boldsymbol{N} = \frac{\frac{\partial f}{\partial \boldsymbol{\sigma}}}{\|\partial f/\partial \boldsymbol{\sigma}\|} = \frac{\mathtt{dev}(\boldsymbol{H}\,\tilde{\boldsymbol{s}}\,\boldsymbol{H})}{\|\mathtt{dev}(\boldsymbol{H}\,\tilde{\boldsymbol{s}}\,\boldsymbol{H})\|} \tag{A.7}$$

This unit normal fulfils the following properties:

$$\boldsymbol{N} : \boldsymbol{N} = 1 \quad \boldsymbol{N} : d\boldsymbol{N} = 0 \tag{A.8}$$

The equivalent plastic strain rate is therefore given by:

$$\dot{\bar{\varepsilon}}^p = \sqrt{\frac{2}{3}\boldsymbol{D}^p : \boldsymbol{D}^p} = \Lambda\sqrt{\frac{2}{3}\boldsymbol{N} : \boldsymbol{N}} = \sqrt{\frac{2}{3}}\Lambda \tag{A.9}$$

We also define $\boldsymbol{n}$ as:

$$\boldsymbol{n} = \mathtt{dev}(\boldsymbol{H}\,\tilde{\boldsymbol{s}}\,\boldsymbol{H}) = \mathbb{M} : \tilde{\boldsymbol{s}} \tag{A.10}$$

Using (A.7), this results in:

$$\boldsymbol{N} = \frac{\mathbb{M} : \tilde{\boldsymbol{s}}}{\|\mathbb{M} : \tilde{\boldsymbol{s}}\|} = \frac{\boldsymbol{n}}{\|\boldsymbol{n}\|} \tag{A.11}$$

Appendix B. Solving the plastic problem

The equations that drive the plastic update are as follows (Eqs. (24) and (26))

$$\tilde{\boldsymbol{s}}^{n+1} = \tilde{\boldsymbol{s}}^e - 2G\gamma\mathbb{M} : \tilde{\boldsymbol{s}}^{n+1} \tag{B.1}$$

$$\bar{\varepsilon}^{p,d}_{n+1} = \bar{\varepsilon}^{p,d}_n + \sqrt{\frac{2}{3}}\gamma\|\tilde{\boldsymbol{s}}^{n+1}\| \tag{B.2}$$

and the update of the plastic multiplier in the Newton–Raphson process can be written:

$$\Delta\gamma = -\frac{r_i}{\left.\frac{\partial \bar{\sigma}^{vM}_{eq}}{\partial\gamma}\right|_{\gamma=\gamma_i} - \left.\frac{\partial \sigma_y}{\partial\gamma}\right|_{\gamma=\gamma_i}} \tag{B.3}$$

The first Eq. (B.1) is a linear system in $\tilde{\boldsymbol{s}}$. It can be written in the form:

$$\mathbb{P} : \tilde{\boldsymbol{s}}^{n+1} = \tilde{\boldsymbol{s}}^e \tag{B.4}$$

[4] This assumption is valid considering a staggered scheme of integration for the coupled plastic/damage problem.
[5] The symmetry of $\boldsymbol{H}$ has to be ensured by its initial symmetry and a symmetric evolution function.

where

$$\mathbb{P}_{ijkl} = \frac{1}{2}(\delta_{ik}\delta_{jl} + \delta_{il}\delta_{jk}) + 2G\gamma\mathbb{M}_{ijkl} = \mathbb{P}(\gamma, \boldsymbol{H})$$

The solution to this system is:

$$\tilde{\boldsymbol{s}}^{n+1} = \mathbb{S} : \tilde{\boldsymbol{s}}^{e} \tag{B.5}$$

where $\mathbb{S}$ is the inverse of $\mathbb{P}$. Notice however that $\mathbb{P}$ is not actually inverted. $\mathbb{S}$ is used as a notation, a linear system has to be solved to compute $\tilde{\boldsymbol{s}}^{n+1}$.

The update of the plastic multiplier (B.3) requires to compute $\left.\frac{\partial \bar{\sigma}_{eq}^{vM\ n+1}}{\partial\gamma}\right|_{\gamma=\gamma_i}$ and $\left.\frac{\partial \sigma_y^{n+1}}{\partial\gamma}\right|_{\gamma=\gamma_i}$.

$$\frac{\partial \bar{\sigma}_{eq}^{vM\ n+1}}{\partial\gamma} = \sqrt{\frac{3}{2}}\frac{1}{\bar{\sigma}_{eq}^{vM\ n+1}}\tilde{\boldsymbol{s}}^{n+1} : \frac{\partial \tilde{\boldsymbol{s}}^{n+1}}{\partial\gamma} = -\sqrt{\frac{3}{2}}\frac{2G}{\bar{\sigma}_{eq}^{vM\ n+1}}\tilde{\boldsymbol{s}}^{n+1} : \left(\mathbb{S} : \boldsymbol{n}^{n+1}\right) \tag{B.6}$$

The latest equality is valid since (derivation of (B.4) with respect to γ):

$$\frac{\partial \mathbb{P} : \tilde{\boldsymbol{s}}^{n+1}}{\partial\gamma} = 0 = \frac{\partial \mathbb{P}}{\partial\gamma} : \tilde{\boldsymbol{s}}^{n+1} + \mathbb{P} : \frac{\partial \tilde{\boldsymbol{s}}^{n+1}}{\partial\gamma} = 2G\boldsymbol{n} + \mathbb{P} : \frac{\partial \tilde{\boldsymbol{s}}^{n+1}}{\partial\gamma}$$

Thus

$$\mathbb{P} : \frac{\partial \tilde{\boldsymbol{s}}^{n+1}}{\partial\gamma} = -2G\boldsymbol{n} \tag{B.7}$$

or,

$$\frac{\partial \tilde{\boldsymbol{s}}^{n+1}}{\partial\gamma} = -2G\mathbb{S} : \boldsymbol{n} \tag{B.8}$$

for which, once more, the latest equality is only a notation, a linear system has to be solved to compute $\frac{\partial \tilde{\boldsymbol{s}}^{n+1}}{\partial\gamma}$.

The last assumption to solve the plastic problem is to use only an isotropic hardening law for the yield limit:

$$\sigma_y(\bar{\varepsilon}^{p,d}) = \sigma_y^0 + h\bar{\varepsilon}^{p,d} \quad \text{thus} \quad \sigma_y^{n+1} = \sigma_y^n + h(\bar{\varepsilon}_{n+1}^{p,d} - \bar{\varepsilon}_n^{p,d})$$

with h the hardening parameter: $h = \frac{d\sigma_y}{d\bar{\varepsilon}^{p,d}}$. We thus have

$$\frac{\partial \sigma_y^{n+1}}{\partial\gamma} = h\frac{\partial(\bar{\varepsilon}_{n+1}^{p,d} - \bar{\varepsilon}_n^{p,d})}{\partial\gamma} \overset{\text{(Eqs. (26) and (B.8))}}{=} \sqrt{\frac{2}{3}}h\left(\|\tilde{\boldsymbol{s}}^{n+1}\| - \frac{2G\gamma}{\|\tilde{\boldsymbol{s}}^{n+1}\|}\tilde{\boldsymbol{s}}^{n+1} : \left[\mathbb{S} : \boldsymbol{n}^{n+1}\right]\right) \tag{B.9}$$

Finally, the update of the plastic multiplier is given by combining (B.3), (B.6), and (B.9):

$$\Delta\gamma = \frac{\|\tilde{\boldsymbol{s}}^{n+1}\| - \sqrt{\frac{2}{3}}\sigma_y(\gamma_i, \tilde{\boldsymbol{s}}^{n+1})}{\frac{2G}{\bar{\sigma}_{eq}^{n+1}}\tilde{\boldsymbol{s}}^{n+1} : [\mathbb{S}(\gamma_i) : \boldsymbol{n}^{n+1}] + \frac{2}{3}h\left(\|\tilde{\boldsymbol{s}}^{n+1}\| - \frac{2G\gamma_i}{\|\tilde{\boldsymbol{s}}^{n+1}\|}\tilde{\boldsymbol{s}}^{n+1} : [\mathbb{S}(\gamma_i) : \boldsymbol{n}^{n+1}]\right)}$$

Once more, we should insist on the fact that $\mathbb{S}$ is used only as a notation. At each iteration of the Newton–Raphson procedure used to compute the plastic multiplier, two linear systems have to be solved to get $\tilde{\boldsymbol{s}}^{n+1}$ (B.4) and $\frac{\partial \tilde{\boldsymbol{s}}^{n+1}}{\partial\gamma}$ (B.7).

Appendix C. Computation of a consistent material tangent stiffness operator

This appendix relates the details of the equations needed to derive the consistent tangent operator for the proposed integration procedure.

The material tangent stiffness operator can be written:

$$\mathbb{H} = \frac{d\boldsymbol{\sigma}}{d\boldsymbol{E}^N} = \mathbb{H}^{vol.} + \mathbb{H}^{dev.} = \boldsymbol{I} \otimes \frac{dp}{d\boldsymbol{E}^N} + \frac{d\boldsymbol{s}}{d\boldsymbol{E}^N} \tag{C.1}$$

with $\mathbb{H}^{vol.}$ and $\mathbb{H}^{dev.}$ the volumic and deviatoric parts of the tangent stiffness operator and $\boldsymbol{\sigma} = \mathbb{M}^{-1} : \tilde{\boldsymbol{\sigma}}$ and $\tilde{\boldsymbol{\sigma}} = \tilde{\boldsymbol{\sigma}}(\boldsymbol{E}^N, \boldsymbol{H}, \gamma)$:

$$\begin{cases} \mathbb{H}^{vol.} = \boldsymbol{I} \otimes \left(\tilde{p}\frac{\partial(1-\eta d^H)}{\partial \boldsymbol{H}} : \frac{d\boldsymbol{H}}{d\boldsymbol{E}^N} + (1-\eta d^H)\frac{\partial \tilde{p}}{\partial \boldsymbol{E}^N}\right) \\ \mathbb{H}^{dev.} = \frac{\partial \boldsymbol{s}}{\partial \boldsymbol{E}^N} + \frac{\partial \boldsymbol{s}}{\partial \boldsymbol{H}} : \frac{d\boldsymbol{H}}{d\boldsymbol{E}^N} + \frac{\partial \boldsymbol{s}}{\partial\gamma} \otimes \frac{d\gamma}{d\boldsymbol{H}} \end{cases} \tag{C.2}$$

with $\boldsymbol{H} = \boldsymbol{H}_0 + \boldsymbol{g}, \tilde{p} = \tilde{p}(J)$ with $J = \mathrm{tr}\left(\boldsymbol{E}^N\right)$ and $\boldsymbol{s} = \boldsymbol{s}(\widehat{\boldsymbol{E}}^N, \gamma, \boldsymbol{H})$

$$\begin{cases} \mathbb{H}^{vol.} = \boldsymbol{I} \otimes \left(-\frac{\eta}{3}\tilde{p}\frac{\partial \mathrm{tr}(\boldsymbol{d})}{\partial \boldsymbol{H}} : \frac{d\boldsymbol{H}}{d\boldsymbol{E}^N} + (1-\eta d^H)\frac{\partial \tilde{p}}{\partial \boldsymbol{E}^N}\right) \\ \mathbb{H}^{dev.} = \mathbb{M}^{-1} : \frac{\partial \tilde{\boldsymbol{s}}}{\partial \boldsymbol{E}^N} + \left(\frac{\partial \mathbb{M}^{-1}}{\partial \boldsymbol{H}} : \tilde{\boldsymbol{s}} + \mathbb{M}^{-1} : \frac{\partial \tilde{\boldsymbol{s}}}{\partial \boldsymbol{H}}\right) : \frac{d\boldsymbol{H}}{d\boldsymbol{E}^N} + \mathbb{M}^{-1} : \frac{\partial \tilde{\boldsymbol{s}}}{\partial\gamma} \otimes \frac{d\gamma}{d\boldsymbol{E}^N} \end{cases} \tag{C.3}$$

C.1. Stress tensor partial derivative

One gets, almost trivially for the partial derivatives with respect to $\boldsymbol{E}^N$ (see Appendix B for the details on the derivative with respect to γ – the derivative with respect to $\boldsymbol{H}$ is computed in the same way.):

$$\frac{\partial \tilde{p}}{\partial \boldsymbol{E}^N} = \frac{\partial \tilde{p}}{\partial J}\frac{\partial J}{\partial \boldsymbol{E}^N} = K\frac{\partial J}{\partial \boldsymbol{E}^N} \tag{C.4}$$

$$\frac{\partial \tilde{\boldsymbol{s}}}{\partial \boldsymbol{E}^N} = \frac{\partial \tilde{\boldsymbol{s}}}{\partial \widehat{\boldsymbol{E}}^N} : \frac{\partial \widehat{\boldsymbol{E}}^N}{\partial \boldsymbol{E}^N} \tag{C.5}$$

$$= 2G\mathbb{S} : \frac{\partial \widehat{\boldsymbol{E}}^N}{\partial \boldsymbol{E}^N} \tag{C.6}$$

with

$$\begin{cases} \frac{\partial J}{\partial \boldsymbol{E}^N} = \boldsymbol{I} \\ \frac{\partial \widehat{\boldsymbol{E}}^N}{\partial \boldsymbol{E}^N} = \mathbb{1} \end{cases} \tag{C.7}$$

C.2. Computation of $\frac{d\gamma}{d\boldsymbol{E}^N}$ (isotropic hardening only)

The derivation of $\frac{d\gamma}{d\boldsymbol{E}^N}$ uses the stationarity property of the yield function: $\frac{df}{d\boldsymbol{E}^N} = 0$.

$$\frac{df}{d\boldsymbol{E}^N} = 0 \tag{C.8}$$

$$= \frac{d\tilde{\sigma}_{eq}{}^{vM}(\tilde{\boldsymbol{s}})}{d\boldsymbol{E}^N} - \frac{d\sigma_y(\tilde{\boldsymbol{s}},\gamma)}{d\boldsymbol{E}^N} \tag{C.9}$$

$$= \left(\frac{\partial \tilde{\sigma}_{eq}^{vM}}{\partial \tilde{\boldsymbol{s}}} - \frac{\partial \sigma_y}{\partial \tilde{\boldsymbol{s}}}\right) : \frac{d\tilde{\boldsymbol{s}}}{d\boldsymbol{E}^N} - \frac{\partial \sigma_y}{\partial \gamma}\frac{d\gamma}{d\boldsymbol{E}^N} \tag{C.10}$$

with:

$$\frac{\partial \tilde{\sigma}_{eq}^{vM}}{\partial \tilde{\boldsymbol{s}}} = \sqrt{\frac{3}{2}}\frac{\tilde{\boldsymbol{s}}}{\|\tilde{\boldsymbol{s}}\|} \tag{C.11}$$

$$\frac{\partial \sigma_y}{\partial \tilde{\boldsymbol{s}}} = \sqrt{\frac{2}{3}}h\gamma\frac{\tilde{\boldsymbol{s}}}{\|\tilde{\boldsymbol{s}}\|} \tag{C.12}$$

$$\frac{\partial \sigma_y}{\partial \gamma} = \sqrt{\frac{2}{3}}h\|\tilde{\boldsymbol{s}}\| \tag{C.13}$$

$$\frac{d\tilde{\boldsymbol{s}}}{d\boldsymbol{E}^N} = \frac{\partial \tilde{\boldsymbol{s}}}{\partial \boldsymbol{E}^N} + \frac{\partial \tilde{\boldsymbol{s}}}{\partial \boldsymbol{H}} : \frac{d\boldsymbol{H}}{d\boldsymbol{E}^N} + \frac{\partial \tilde{\boldsymbol{s}}}{\partial \gamma} \otimes \frac{d\gamma}{d\boldsymbol{E}^N} \tag{C.14}$$

One therefore gets:

$$\left(\sqrt{\frac{3}{2}} - \sqrt{\frac{2}{3}}h\gamma\right)\frac{\tilde{\boldsymbol{s}}}{\|\tilde{\boldsymbol{s}}\|} : \frac{d\tilde{\boldsymbol{s}}}{d\boldsymbol{E}^N} - \sqrt{\frac{2}{3}}h\|\tilde{\boldsymbol{s}}\|\frac{d\gamma}{d\boldsymbol{E}^N} = 0$$

which leads to:

$$\sqrt{\frac{3}{2}}\frac{\tilde{\boldsymbol{s}}}{\|\tilde{\boldsymbol{s}}\|} : \left(\frac{\partial \tilde{\boldsymbol{s}}}{\partial \boldsymbol{E}^N} + \frac{\partial \tilde{\boldsymbol{s}}}{\partial \gamma} \otimes \frac{d\gamma}{d\boldsymbol{E}^N} + \frac{\partial \tilde{\boldsymbol{s}}}{\partial \boldsymbol{H}} : \frac{d\boldsymbol{H}}{d\boldsymbol{E}^N}\right) - h\sqrt{\frac{2}{3}}\left(\|\tilde{\boldsymbol{s}}\|\frac{d\gamma}{d\boldsymbol{E}^N} + \gamma\frac{\tilde{\boldsymbol{s}}}{\|\tilde{\boldsymbol{s}}\|} : \left(\frac{\partial \tilde{\boldsymbol{s}}}{\partial \boldsymbol{E}^N} + \frac{\partial \tilde{\boldsymbol{s}}}{\partial \gamma} \otimes \frac{d\gamma}{d\boldsymbol{E}^N} + \frac{\partial \tilde{\boldsymbol{s}}}{\partial \boldsymbol{H}} : \frac{d\boldsymbol{H}}{d\boldsymbol{E}^N}\right)\right) = 0 \tag{C.15}$$

The terms of this equation can be re-arranged to obtain an equation for $\frac{d\gamma}{d\boldsymbol{E}^N}$:

$$\left[\left(\sqrt{\frac{3}{2}} - h\sqrt{\frac{2}{3}}\gamma\right)\frac{\tilde{\boldsymbol{s}}}{\|\tilde{\boldsymbol{s}}\|} : \frac{\partial \tilde{\boldsymbol{s}}}{\partial \gamma} - h\sqrt{\frac{2}{3}}\|\tilde{\boldsymbol{s}}\|\right]\frac{d\gamma}{d\boldsymbol{E}^N} = h\sqrt{\frac{2}{3}}\gamma\frac{\tilde{\boldsymbol{s}}}{\|\tilde{\boldsymbol{s}}\|} : \left(\frac{\partial \tilde{\boldsymbol{s}}}{\partial \boldsymbol{E}^N} + \frac{\partial \tilde{\boldsymbol{s}}}{\partial \boldsymbol{H}} : \frac{d\boldsymbol{H}}{d\boldsymbol{E}^N}\right) - \sqrt{\frac{3}{2}}\frac{\tilde{\boldsymbol{s}}}{\|\tilde{\boldsymbol{s}}\|} : \left(\frac{\partial \tilde{\boldsymbol{s}}}{\partial \boldsymbol{E}^N} + \frac{\partial \tilde{\boldsymbol{s}}}{\partial \boldsymbol{H}} : \frac{d\boldsymbol{H}}{d\boldsymbol{E}^N}\right) \tag{C.16}$$

This gives

$$\frac{d\gamma}{d\boldsymbol{E}^N} = \boldsymbol{\alpha} + \boldsymbol{\zeta} : \frac{d\boldsymbol{H}}{d\boldsymbol{E}^N} \tag{C.17}$$

with

$$\boldsymbol{\alpha} = \frac{1}{\text{den}}\left(\boldsymbol{A}_1 : \frac{\partial \tilde{\boldsymbol{s}}}{\partial \boldsymbol{E}^N}\right) \tag{C.18}$$

$$\zeta = \frac{1}{\text{den}}\left(\boldsymbol{A}_1 : \frac{\partial \tilde{\boldsymbol{s}}}{\partial \boldsymbol{H}}\right) \tag{C.19}$$

and

$$\boldsymbol{A}_1 = \left(h\sqrt{\frac{2}{3}}\gamma - \sqrt{\frac{3}{2}}\right)\frac{\tilde{\boldsymbol{s}}}{\|\tilde{\boldsymbol{s}}\|} \tag{C.20}$$

$$\text{den} = -\boldsymbol{A}_1 : \frac{\partial \tilde{\boldsymbol{s}}}{\partial \gamma} - h\sqrt{\frac{2}{3}}\|\tilde{\boldsymbol{s}}\| \tag{C.21}$$

C.3. Computation of $\frac{d\boldsymbol{H}}{d\boldsymbol{E}^N}$

The derivative of $\boldsymbol{H}$ with respect to the natural strain ($\boldsymbol{E}^N$) depends explicitly on the damage evolution law (terms written as $\frac{\partial \boldsymbol{g}}{\partial \cdot}$):

$$\frac{d\boldsymbol{H}}{d\boldsymbol{E}^N} = \frac{d\boldsymbol{g}}{d\boldsymbol{E}^N} = \frac{\partial \boldsymbol{g}}{\partial \boldsymbol{E}^N} + \frac{\partial \boldsymbol{g}}{\partial \boldsymbol{s}} : \frac{d\boldsymbol{s}}{d\boldsymbol{E}^N} + \frac{\partial \boldsymbol{g}}{\partial p} \otimes \frac{dp}{d\boldsymbol{E}^N} + \frac{\partial \boldsymbol{g}}{\partial \boldsymbol{H}} : \frac{d\boldsymbol{H}}{d\boldsymbol{E}^N} + \frac{\partial \boldsymbol{g}}{\partial \gamma} \otimes \frac{d\gamma}{d\boldsymbol{E}^N} \tag{C.22}$$

Using (C.2) and (C.17) allows one to write (C.22) as:

$$\left[\boldsymbol{I} \underline{\otimes} \boldsymbol{I} - \frac{\partial \boldsymbol{g}}{\partial \boldsymbol{s}} : \left(\frac{\partial \boldsymbol{s}}{\partial \gamma} \otimes \boldsymbol{\zeta} + \frac{\partial \boldsymbol{s}}{\partial \boldsymbol{H}}\right) - \frac{\partial \boldsymbol{g}}{\partial p} \otimes \frac{\partial p}{\partial \boldsymbol{H}} - \frac{\partial \boldsymbol{g}}{\partial \boldsymbol{H}} - \frac{\partial \boldsymbol{g}}{\partial \gamma} \otimes \boldsymbol{\zeta}\right] : \frac{d\boldsymbol{H}}{d\boldsymbol{E}^N} = \frac{\partial \boldsymbol{g}}{\partial \boldsymbol{E}^N} + \frac{\partial \boldsymbol{g}}{\partial \boldsymbol{s}} : \left(\frac{\partial \boldsymbol{s}}{\partial \boldsymbol{E}^N} + \frac{\partial \tilde{\boldsymbol{s}}}{\partial \gamma} \otimes \boldsymbol{\alpha}\right) + \frac{\partial \boldsymbol{g}}{\partial p} \otimes \frac{dp}{d\boldsymbol{E}^N} + \frac{\partial \boldsymbol{g}}{\partial \gamma} \otimes \boldsymbol{\alpha} \tag{C.23}$$

where all the derivatives both on the left and right hand side of the equation are known.

This equation is generically written $A_{ijkl}X_{klmn} = B_{ijmn}$ where A and B are known. This system solution can be broken down solving 9 equations of the type $A_{ijkl}x_{kl} = b_{ij}$ which are systems of 9 linear equations in x_{kl}.

C.4. Derivatives of $\mathbb{M}$ and $\mathbb{M}^{-1}$

Derivatives of $\mathbb{M}$ and $\mathbb{M}^{-1}$ with respect to damage remain to be computed. These are in general sixth order tensors. However, in the computation of the stiffness operator, the general sixth order tensors are not needed. Only the fourth order tensors $\frac{\partial \mathbb{M}}{\partial \boldsymbol{H}} : \tilde{\boldsymbol{s}}$, $\frac{\partial \mathbb{M}^{-1}}{\partial \boldsymbol{H}} : \tilde{\boldsymbol{s}}$ as well as $\frac{\partial \mathrm{tr}(\boldsymbol{d})}{\partial \boldsymbol{H}}$ are to be computed.

C.4.1. Computation of $\frac{\partial \mathbb{M}}{\partial \boldsymbol{H}} : \tilde{\boldsymbol{s}}$

$$[\mathbb{M} : \tilde{\boldsymbol{s}}]_{ij} = [\mathtt{dev}(\boldsymbol{H}\,\tilde{\boldsymbol{s}}\,\boldsymbol{H})]_{ij} = [\boldsymbol{H}\,\tilde{\boldsymbol{s}}\,\boldsymbol{H}]_{ij} - \frac{1}{3}[\boldsymbol{H}\,\tilde{\boldsymbol{s}}\,\boldsymbol{H}]_{nn}\delta_{ij}$$

Therefore

$$\left.\frac{\partial [\mathbb{M} : \tilde{\boldsymbol{s}}]_{ij}}{\partial H_{kl}}\right|_{\tilde{\boldsymbol{s}}\ \text{cst}} = \delta_{ik}[\boldsymbol{H}\tilde{\boldsymbol{s}}]_{jl} + \delta_{jl}[\boldsymbol{H}\tilde{\boldsymbol{s}}]_{ik} - \frac{1}{3}\left([\boldsymbol{H}\tilde{\boldsymbol{s}}]_{kl} + [\boldsymbol{H}\tilde{\boldsymbol{s}}]_{lk}\right)\delta_{ij} \tag{C.24}$$

$$\frac{\partial \mathbb{M}}{\partial \boldsymbol{H}} : \tilde{\boldsymbol{s}} = \boldsymbol{I}\underline{\otimes}(\boldsymbol{H}\tilde{\boldsymbol{s}}) + (\boldsymbol{H}\tilde{\boldsymbol{s}})\underline{\otimes}\boldsymbol{I} - \frac{1}{3}\boldsymbol{I} \otimes \left[(\boldsymbol{H}\tilde{\boldsymbol{s}}) + (\boldsymbol{H}\tilde{\boldsymbol{s}})^T\right] \tag{C.25}$$

C.4.2. Computation of $\frac{\partial \mathbb{M}^{-1}}{\partial \boldsymbol{H}} : \tilde{\boldsymbol{s}}$

$$\left[\mathbb{M}^{-1} : \tilde{\boldsymbol{s}}\right]_{ij} = \underbrace{(H^{-1})_{io}\tilde{s}_{op}(H^{-1})_{pj}}_{\star_{ij}} - \underbrace{\frac{H_{ij}^{-2}(\tilde{s}_{mn}H_{mn}^{-2})}{\mathrm{tr}\left(\boldsymbol{H}^{-2}\right)}}_{\star\star_{ij}} \tag{C.26}$$

One has

$$\left.\frac{\partial \star_{ij}}{\partial H_{kl}}\right|_{\tilde{\boldsymbol{s}}\ \text{cst}} = \frac{\partial H_{io}^{-1}}{\partial H_{kl}}\tilde{s}_{op}H_{pj}^{-1} + H_{io}^{-1}\tilde{s}_{op}\frac{\partial H_{pj}^{-1}}{\partial H_{kl}} = -H_{ik}^{-1}\left(H^{-1}\tilde{s}H^{-1}\right)_{jl} - \left(H^{-1}\tilde{s}H^{-1}\right)_{ik}H_{jl}^{-1}$$

and

$$\left.\frac{\partial \star\star_{ij}}{\partial H_{kl}}\right|_{\tilde{\boldsymbol{s}}\ \text{cst}} = \frac{\partial H_{ij}^{-2}}{\partial H_{kl}}\frac{\tilde{s}_{mn}H_{mn}^{-2}}{\mathrm{tr}\left(\boldsymbol{H}^{-2}\right)} + H_{ij}^{-2}\frac{\tilde{s}_{mn}}{\mathrm{tr}\left(\boldsymbol{H}^{-2}\right)}\frac{\partial H_{mn}^{-2}}{\partial H_{kl}} - \frac{H_{ij}^{-2}\tilde{s}_{mn}H_{mn}^{-2}}{\left(\mathrm{tr}\left(\boldsymbol{H}^{-2}\right)\right)^2}\frac{\partial \mathrm{tr}\left(\boldsymbol{H}^{-2}\right)}{\partial H_{kl}}$$

with

$$\frac{\partial H^{-2}_{ij}}{\partial H_{kl}} = \frac{\partial H^{-1}_{io}}{\partial H_{kl}} H^{-1}_{oj} + H^{-1}_{io} \frac{\partial H^{-1}_{oj}}{\partial H_{kl}} = -(H^{-1}_{ik} H^{-2}_{jl} + H^{-2}_{ik} H^{-1}_{jl})$$

$$\frac{\partial \boldsymbol{H}^{-2}}{\partial \boldsymbol{H}} = -(\boldsymbol{H}^{-2} \underline{\otimes} \boldsymbol{H}^{-1} + \boldsymbol{H}^{-1} \underline{\otimes} \boldsymbol{H}^{-2})$$

and

$$\frac{\partial \mathrm{tr}\left(\boldsymbol{H}^{-2}\right)}{\partial \boldsymbol{H}} = \frac{\partial \boldsymbol{H}^{-2} : \boldsymbol{I}}{\partial \boldsymbol{H}} = -2\boldsymbol{H}^{-3}$$

One can therefore write

$$\left.\frac{\partial \bigstar\bigstar_{ij}}{\partial H_{kl}}\right|_{\tilde{\boldsymbol{s}}\ \mathrm{cst}} = -\left[\left(H^{-1}_{ik} H^{-2}_{jl} + H^{-2}_{ik} H^{-1}_{jl}\right) \frac{\tilde{s}_{mn} H^{-2}_{mn}}{\mathrm{tr}\left(\boldsymbol{H}^{-2}\right)} + \frac{H^{-2}_{ij}}{\mathrm{tr}\left(\boldsymbol{H}^{-2}\right)} \left([\boldsymbol{H}^{-1}\tilde{\boldsymbol{s}}\boldsymbol{H}^{-2}]_{kl} + [\boldsymbol{H}^{-2}\tilde{\boldsymbol{s}}\boldsymbol{H}^{-1}]_{kl}\right) - H^{-2}_{ij} \frac{2\tilde{s}_{mn} H^{-2}_{mn}}{\left(\mathrm{tr}\left(\boldsymbol{H}^{-2}\right)\right)^2} H^{-3}_{kl}\right]$$

Finally the fourth order tensor $\frac{\partial \mathbb{M}^{-1} : \tilde{\boldsymbol{s}}}{\partial \boldsymbol{H}}$ can be written:

$$\frac{\partial M^{-1}_{ijop}}{\partial H_{kl}} \tilde{s}_{op} = -H^{-1}_{ik} \left(H^{-1}\tilde{s}H^{-1}\right)_{jl} - \left(H^{-1}\tilde{s}H^{-1}\right)_{ik} H^{-1}_{jl} + \frac{\tilde{s}_{mn} H^{-2}_{mn}}{\mathrm{tr}\left(\boldsymbol{H}^{-2}\right)} \left[H^{-1}_{ik} H^{-2}_{jl} + H^{-2}_{ik} H^{-1}_{jl} - \frac{2}{\mathrm{tr}\left(\boldsymbol{H}^{-2}\right)} H^{-2}_{ij} H^{-3}_{kl}\right]$$
$$+ \frac{H^{-2}_{ij}}{\mathrm{tr}\left(\boldsymbol{H}^{-2}\right)} \left([\boldsymbol{H}^{-1}\tilde{\boldsymbol{s}}\boldsymbol{H}^{-2}]_{kl} + [\boldsymbol{H}^{-2}\tilde{\boldsymbol{s}}\boldsymbol{H}^{-1}]_{kl}\right) \tag{C.27}$$

or else

$$\frac{\partial \mathbb{M}^{-1}}{\partial \boldsymbol{H}} : \tilde{\boldsymbol{s}} = -\boldsymbol{H}^{-1} \underline{\otimes} \left(\boldsymbol{H}^{-1}\tilde{\boldsymbol{s}}\boldsymbol{H}^{-1}\right) - \left(\boldsymbol{H}^{-1}\tilde{\boldsymbol{s}}\boldsymbol{H}^{-1}\right) \underline{\otimes} \boldsymbol{H}^{-1} + \frac{\tilde{\boldsymbol{s}} : \boldsymbol{H}^{-2}}{\mathrm{tr}\left(\boldsymbol{H}^{-2}\right)} \left[\boldsymbol{H}^{-1} \underline{\otimes} \boldsymbol{H}^{-2} + \boldsymbol{H}^{-2} \underline{\otimes} \boldsymbol{H}^{-1} - \frac{2}{\mathrm{tr}\left(\boldsymbol{H}^{-2}\right)} \boldsymbol{H}^{-2} \otimes \boldsymbol{H}^{-3}\right]$$
$$+ \frac{\boldsymbol{H}^{-2}}{\mathrm{tr}\left(\boldsymbol{H}^{-2}\right)} \otimes \left[\boldsymbol{H}^{-1}\tilde{\boldsymbol{s}}\boldsymbol{H}^{-2} + \boldsymbol{H}^{-2}\tilde{\boldsymbol{s}}\boldsymbol{H}^{-1}\right] \tag{C.28}$$

C.4.3. Computation of $\frac{\partial \mathrm{tr}(\boldsymbol{d})}{\partial \boldsymbol{H}}$

As $\boldsymbol{d} = \boldsymbol{I} - \boldsymbol{H}^{-2}$ and as, for any invertible symmetric tensor such as $\boldsymbol{H}$, one has: $\frac{\partial \boldsymbol{H}^{-1}}{\partial \boldsymbol{H}} = -\boldsymbol{H}^{-1} \underline{\otimes} \boldsymbol{H}^{-1}$, so that one can write:

$$\frac{\partial \boldsymbol{d}}{\partial \boldsymbol{H}} = \boldsymbol{H}^{-2} \underline{\otimes} \boldsymbol{H}^{-1} + \boldsymbol{H}^{-1} \underline{\otimes} \boldsymbol{H}^{-2} \tag{C.29}$$

The computation of $\frac{\partial \mathrm{tr}(\boldsymbol{d})}{\partial \boldsymbol{H}}$ is therefore directly given by:

$$\frac{\partial \mathrm{tr}(\boldsymbol{d})}{\partial \boldsymbol{H}} = \frac{\partial \boldsymbol{d}}{\partial \boldsymbol{H}} : \boldsymbol{I} = \left(\boldsymbol{H}^{-2} \underline{\otimes} \boldsymbol{H}^{-1} + \boldsymbol{H}^{-1} \underline{\otimes} \boldsymbol{H}^{-2}\right) : \boldsymbol{I} = 2\boldsymbol{H}^{-3} \tag{C.30}$$

As $\boldsymbol{H}$ is a polynomial function of $\boldsymbol{d}$, the derivative given by C.29 can be computed by the use of a spectral decomposition of $\boldsymbol{d}$.

References

Aboudi, J., 2011. The effect of anisotropic damage evolution on the behavior of ductile and brittle matrix composites. Int. J. Solids Struct. 48, 2102–2119.

Abu Al Rub, R.K., Darabi, M.K., 2012. A thermodynamic framework for constitutive modeling of time- and rate-dependent materials. Part I: Theory. Int. J. Plast. 34, 61–92.

Abu Al-Rub, R.K., Voyiadjis, G.Z., 2003. On the coupling of anisotropic damage and plasticity models for ductile materials. Int. J. Solids Struct. 40, 2611–2643.

Abu Al Rub, R.K., Voyiadjis, G.Z., 2006. A finite strain plastic-damage model for high velocity impact using combined viscosity and gradient localization limiters: Part I-theoretical formulation. Int. J. Damage Mech. 15, 293–334.

Badreddine, H., Saanouni, K., Dogui, A., 2010. On non-associative anisotropic finite plasticity fully coupled with isotropic ductile damage for metal forming. Int. J. Plast. 26, 1541–1575.

Balzani, D., Brinkhues, S., Holzapfel, G.A., 2012. Constitutive framework for the modeling of damage in collagenous soft tissues with application to arterial walls. Comput. Methods Appl. Mech. Eng., 139–151.

Bayraktar, H.H., Keaveny, T.M., 2004. Mechanisms of uniformity of yield strains for trabecular bone. J. Biomech. 37, 1671–1678.

Beaupré, G.S., Orr, T.E., Carter, D.R., 1990. An approach for time-dependent bone modeling and remodeling-theoretical development. J. Orthop. Res. 8, 651–661.

Bernick, K.B., Prevost, T.P., Suresh, S., Socrate, S., 2011. Biomechanics of single cortical neurons. Acta Biomater. 7, 1210–1219.

Besson, J., 2009. Damage of ductile materials deforming under multiple plastic or viscoplastic mechanisms. Int. J. Plast. 25, 2204–2221.

Besson, J., 2010. Continuum models of ductile fracture: a review. Int. J. Damage Mech. 19, 3–52.

Boers, S., Schreurs, P., Geers, M., 2005. Operator-split damage-plasticity applied to groove forming in food can lids. Int. J. Solids Struct. 42, 4154–4178.
Bonora, N., Ruggiero, A., Esposito, L., Gentile, D., 2006. CDM modeling of ductile failure in ferritic steels: assessment of the geometry transferability of model parameters. Int. J. Plast. 22, 2015–2047.
Borgqvist, E., Wallin, M., 2013. Numerical integration of elasto-plasticity coupled to damage using a diagonal implicit Runge–Kutta integration scheme. Int. J. Damage Mech. 22, 68–94.
Boryor, A., Hohmann, A., Geiger, M., Wolfram, U., Sander, C., Sander, F.G., 2009. A downloadable meshed human canine tooth model with PDL and bone for finite element simulations. Dental Mater. 25, e57–e62.
Bourauel, C., Vollmer, D., Jäger, A., 2000. Application of bone remodeling theories in the simulation of orthodontic tooth movements. J. Orofac. Orthop. 61, 266–279.
Brodland, G.W., Chen, D.I.L., Veldhuis, J.H., 2006. A cell-based constitutive model for embryonic epithelia and other planar aggregates of biological cells. Int. J. Plast. 22, 965–995.
Brünig, M., 2002. Numerical analysis and elastic-plastic deformation behavior of anisotropically damaged solids. Int. J. Plast. 18, 1237–1270.
Brünig, M., 2003a. An anisotropic ductile damage model based on irreversible thermodynamics. Int. J. Plast. 19, 1679–1713.
Brünig, M., 2003b. Numerical analysis of anisotropic ductile continuum damage. Comput. Methods Appl. Mech. Eng. 192, 2949–2976.
Brünig, M., Gerke, S., 2011. Simulation of damage evolution in ductile metals undergoing dynamic loading conditions. Int. J. Plast. 27, 1598–1617.
Brünig, M., Chyra, O., Albrecht, D., Driemeier, L., Alves, M., 2008. A ductile damage criterion at various stress triaxialities. Int. J. Plast. 24, 1731–1755.
Calvo, B., Pea, E., Martins, P., Mascarenhas, T., Doblar, M., Jorge, R.N., Ferreira, A., 2009. On modelling damage process in vaginal tissue. J. Biomech. 42, 642–651.
Cowin, S.C., 1986. Wolff's law of trabecular architecture at remodelling equilibrium. J. Biomech. Eng. 108, 83–88.
Desmorat, R., Otin, S., 2008. Cross-identification isotropic/anisotropic damage and application to anisothermal structural failure. Eng. Fract. Mech. 75, 3446–3463.
de Souza Neto, E., Perić, D., 1996. A computational framework for a class of fully coupled models for elastoplastic damage at finite strains with reference to the linearization aspects. Comput. Methods Appl. Mech. Eng. 130, 179–193.
de Souza Neto, E., Perić, D., Owen, D., 1994. A model for elastoplastic damage at finite strains: algorithmic issues and applications. Eng. Comput. 11, 257–281.
de Souza Neto, E.A., Peric, D., Owen, D.R.J., 2011. Computational Methods for Plasticity: Theory and Applications. John Wiley & Sons.
Doblaré, M., García, J.M., 2002. Anisotropic bone remodelling model based on a continuum damage-repair theory. J. Biomech. 35, 1–17.
Doghri, I., 1995. Numerical implementation and analysis of a class of metal plasticity models coupled with ductile damage. Int. J. Numer. Methods Eng. 38, 3403–3431.
d'Otreppe, V., Boman, R., Ponthot, J.P., 2012. Generating smooth surface meshes from multi-region medical images. Int. J. Numer. Methods Biomed. Eng. 28, 646–660.
Duddu, R., Waisman, H., 2013. A nonlocal continuum damage mechanics approach to simulation of creep fracture in ice sheets. Comput. Mech. 51, 961–974.
Dunand, M., Maertens, A.P., Luo, M., Mohr, D., 2012. Experiments and modeling of anisotropic aluminum extrusions under multi-axial loading – part I: plasticity. Int. J. Plast. 36, 34–49.
Ekh, M., Lillbacka, R., Runesson, K., 2004. A model framework for anisotropic damage coupled to crystal (visco)plasticity. Int. J. Plast. 20, 2143–2159.
El khaoulani, R., Bouchard, P.O., 2013. Efficient numerical integration of an elastic-plastic damage law within a mixed velocity–pressure formulation. Math. Comput. Simul. 94, 145–158.
Frost, H., 1964. The Laws of Bone Structure. Henry Ford Hospital Surgical Monographs.
Frost, H., 1987. Bone mass and the mechanostat: a proposal. Anat. Rec. 219, 1–9.
García, J.M., Doblaré, M., Cegonino, J., 2002. Bone remodelling simulation: a tool for implant design. Comput. Mater. Sci. 25, 100–114.
Garcia, D., Zysset, P.K., Charlebois, M., Curnier, A., 2009. A three-dimensional elastic plastic damage constitutive law for bone tissue. Biomech. Model. Mechanobiol. 8, 149–165.
Guo, S., Kang, G., Zhang, J., 2013. A cyclic visco-plastic constitutive model for time-dependent ratchetting of particle-reinforced metal matrix composites. Int. J. Plast. 40, 101–125.
Gurson, A., 1977. Continuum theory of ductile rupture by void nucleation and growth I. Yield criteria and flow rules for porous ductile media. Trans. ASME Ser. H, J. Eng. Mater. Technol. 99, 2–15.
Hammi, Y., Horstemeyer, M., 2007. A physically motivated anisotropic tensorial representation of damage with separate functions for void nucleation, growth, and coalescence. Int. J. Plast. 23, 1641–1678.
Horstemeyer, M.F., Bammann, D.J., 2010. Historical review of internal state variable theory for inelasticity. Int. J. Plast. 26, 1310–1334.
Horstemeyer, M., Matalanis, M., Sieber, A., Botos, M., 2000. Micromechanical finite element calculations of temperature and void configuration effects on void growth and coalescence. Int. J. Plast. 16, 979–1015.
Hosseini, S., Wilson, W., Ito, K., van Donkelaar, C., 2014. A numerical model to study mechanically induced initiation and progression of damage in articular cartilage. Osteoarthr. Cartilage 22, 95–103.
Jacobs, C.R., 1994. Numerical Simulation of Bone Adaptation to Mechanical Loading. Ph.D. Thesis, Department of Mechanical Engineering – Stanford University.
Jeunechamps, P.P., Ponthot, J.P., 2013. An efficient 3D implicit approach for the thermomechanical simulation of elastic–viscoplastic materials submitted to high strain rate and damage. Int. J. Numer. Methods Eng. 94, 920–960.
Kachanov, L., 1958. Time of the rupture process under creep conditions. TVZ Akad Nauk S.S.R. Otd. Tech. Nauk 8, 26–31.
Khan, A.S., Liu, H., 2012. A new approach for ductile fracture prediction on al 2024-t351 alloy. Int. J. Plast. 35, 1–12.
Kitzig, M., Häußler-Combe, U., 2011. Modeling of plain concrete structures based on an anisotropic damage formulation. Mater. Struct. 44, 1837–1853.
Krishnan, V., Davidovitch, Z., 2009. On a path to unfolding the biological mechanisms of orthodontic tooth movement. J. Dental Res. 88, 597–608.
Lai, Y., Jin, L., Chang, X., 2009. Yield criterion and elasto-plastic damage constitutive model for frozen sandy soil. Int. J. Plast. 25, 1177–1205.
Lecarme, L., Tekoglu, C., Pardoen, T., 2011. Void growth and coalescence in ductile solids with stage III and stage IV strain hardening. Int. J. Plast. 27, 1203–1223.
Lemaitre, J., 1992. A Course on Damage Mechanics Failures. Springer-Verlag.
Lemaitre, J., Desmorat, R., 2005. Engineering Damage Mechanics: Ductile, Creep, Fatigue and Brittle Failures. Springer.
Lemaitre, J., Desmorat, R., Sauzay, M., 2000. Anisotropic damage law of evolution. Eur. J. Mech. – A/Solids 19, 187–208.
Lennon, A., Prendergast, P., 2004. Modelling damage growth and failure in elastic materials with random defect distributions. Math. Proc. Roy. Irish Acad. 104, 155–171.
Lindauer, S., 2001. The basics of orthodontic mechanics. Sem. Orthod. 7, 2–15.
Luo, M., Dunand, M., Mohr, D., 2012. Experiments and modeling of anisotropic aluminum extrusions under multi-axial loading – part II: ductile fracture. Int. J. Plast., 36–58.
Mahnken, R., 2002. Theoretical, numerical and identification aspects of a new model class for ductile damage. Int. J. Plast. 18, 801–831.
Masella, R.S., Chung, P.L., 2008. Thinking beyond the wire: Emerging biologic relationships in orthodontics and periodontology. Sem. Orthod. 14, 290–304, Emerging Concepts in Orthodontic Periodontal Interactions for the 21st Century.
Mashayekhi, M., Ziaei-Rad, S., Parvizian, J., Nikbin, K., Hadavinia, H., 2005. Numerical analysis of damage evolution in ductile solids. Struct. Integrity Durability 1, 67–82.
Melsen, B., 2001. Tissue reaction to orthodontic tooth movement – a new paradigm. Eur. J. Orthod. 23, 671–681.

Mengoni, M., 2012. On the Development of an Integrated Bone Remodeling Law for Orthodontic Tooth Movements Models using the Finite Element Method. PhD Thesis, School of Engineering, University of Liège, Belgium. http://orbi.ulg.ac.be/handle/2268/126082.
Mengoni, M., Ponthot, J.P., 2010. Isotropic continuum damage/repair model for alveolar bone remodeling. J. Comput. Appl. Math. 234, 2036–2045.
Mengoni, M., Voide, R., de Bien, C., Freichels, H., Jérôme, C., Léonard, A., Toye, D., van Lenthe, G.H., Müller, R., Ponthot, J.P., 2012. A non-linear homogeneous model for bone-like materials under compressive load. Int. J. Numer. Methods Biomed. Eng. 28, 334–348.
Menzel, A., Steinmann, P., 2001. A theoretical and computational framework for anisotropic continuum damage mechanics at large strains. Int. J. Solids Struct. 38, 9505–9523.
Menzel, A., Ekh, M., Steinmann, P., Runesson, K., 2002. Anisotropic damage coupled to plasticity: modelling based on the effective configuration concept. Int. J. Numer. Methods Eng. 54, 1409–1430.
Menzel, A., Ekh, M., Runesson, K., Steinmann, P., 2005. A framework for multiplicative elastoplasticity with kinematic hardening coupled to anisotropic damage. Int. J. Plast. 21, 397–434.
Niebur, G.L., Feldstein, M.J., Yuen, J.C., Chen, T.J., Keaveny, T.M., 2000. High-resolution finite element models with tissue strength asymmetry accurately predict failure of trabecular bone. J. Biomech. 33, 1575–1583.
Ponthot, J.P., 2002. Unified stress update algorithms for the numerical simulation of large deformation elasto-plastic and elasto-viscoplastic processes. Int. J. Plast. 18, 91–126.
Qasim, M., Natarajan, R.N., An, H.S., Andersson, G.B., 2014. Damage accumulation location under cyclic loading in the lumbar disc shifts from inner annulus lamellae to peripheral annulus with increasing disc degeneration. J. Biomech. 47, 24–31.
Qi, W., Bertram, A., 1999. Anisotropic continuum damage modeling for single crystals at high temperatures. Int. J. Plast. 15, 1197–1215.
Roberts, W.E., 2000. Bone physiology of tooth movement, ankylosis, and osseointegration. Sem. Orthod. 6, 173–182.
Rabotnov, Y.N. Creep Rupture. In Proceedings of the 12th International Congress of Applied Mechanics (eds M. Hetenyi, W.G. Vincenti) Stanford 1968, Springer Berlin, pp. 342–349.
Rousselier, G., 1987. Ductile fracture models and their potential in local approach of fracture. Nucl. Eng. Des. 105, 97–111.
Shojaei, A., Voyiadjis, G.Z., Tan, P., 2013. Viscoplastic constitutive theory for brittle to ductile damage in polycrystalline materials under dynamic loading. Int. J. Plast. 48, 125–151.
Simo, J., Ju, J., 1987a. Strain-and stress-based continuum damage models I. Formulation. Int. J. Solids Struct. 23, 820–840.
Simo, J., Ju, J., 1987b. Strain-and stress-based continuum damage models II. Computational aspects. Int. J. Solids Struct. 23, 841–869.
Souza, F.V., Allen, D.H., 2012. Computation of homogenized constitutive tensor of elastic solids containing evolving cracks. Int. J. Damage Mech. 21, 267–291.
Stewart, C.M., Gordon, A.P., Ma, Y.W., Neu, R.W., 2011. An anisotropic tertiary creep damage constitutive model for anisotropic materials. Int. J. Pressure Ves. Piping 88, 356–364.
Stölken, J., Kinney, J., 2003. On the importance of geometric nonlinearity in finite-element simulations of trabecular bone failure. Bone 33, 494–504.
Tekoglu, C., Pardoen, T., 2010. A micromechanics based damage model for composite materials. Int. J. Plast. 26, 549–569.
Tvergaard, V., Needleman, A., 1984. Analysis of the cup-cone fracture in a round tensile bar. Acta Metall. 32, 157–169.
Van Schepdael, A., Vander Sloten, J., Geris, L., 2013. A mechanobiological model of orthodontic tooth movement. Biomech. Model. Mechanobiol. 12, 249–265.
Vaz, M., Owen, D.R.J., 2001. Aspects of ductile fracture and adaptive mesh refinement in damaged elasto-plastic materials. Int. J. Numer. Methods Eng. 50, 29–54.
Verhulp, E., van Rietbergen, B., Müller, R., Huiskes, R., 2008. Micro-finite element simulation of trabecular-bone post-yield behaviour – effects of material model, element size and type. Comput. Methods Biomech. Biomed. Eng. 11, 389–395.
Verna, C., Dalstra, M., Lee, T.C., Cattaneo, P.M., Melsen, B., 2004. Microcracks in the alveolar bone following orthodontic tooth movement: a morphological and morphometric study. Eur. J. Orthod. 26, 459–467.
Voyiadjis, G.Z., Kattan, P.I., 2006. Advances in Damage Mechanics: Metals and Metal Matrix Composites with an Introduction to Fabric Tensors, second ed. Elsevier Science Ltd.
Voyiadjis, G.Z., Taqieddin, Z.N., Kattan, P.I., 2008. Anisotropic damage-plasticity model for concrete. Int. J. Plast. 24, 1946–1965.
Zaïri, F., Naït-Abdelaziz, M., Gloaguen, J., Lefebvre, J., 2011. A physically-based constitutive model for anisotropic damage in rubber-toughened glassy polymers during finite deformation. Int. J. Plast. 27, 25–51.
Zapara, M., Tutyshkin, N., Müller, W.H., Wille, R., 2012. Constitutive equations of a tensorial model for ductile damage of metals. Continuum Mech. Thermodyn. 24, 697–717.
Zysset, P., Curnier, A., 1996. A 3D damage model for trabecular bone based on fabric tensors. J. Biomech. 29, 1549–1558.